Numerical simulation of the side launching of a ship

Bobby Hak

Department of Mathematics

RuG

Master's Thesis

Numerical simulation of the side launching of a ship

Bobby Hak

Supervisor:
Prof.dr. A.E.P. Veldman
Department of Mathematics
University of Groningen
P.O. Box 800
9700 AV Groningen

August 2005

Contents

Chapter 1

Introduction

Side launching is a hectic and dynamic process. Once the procedure has begun, there is no stopping it and one can just hope the best. Unfortunately there is a serious risk of the ship getting damaged in the course of action. In shallow water the ship can capsize if the heeling angle is too large. If the ship is launched to slow it will fall back risking its chine hitting the slip way with damage to the bottom of the vessel. Therefore the management until the actual launch is crucial to get a successful launch.

For ages now (uniform) ships have been produced and side launched in the Netherlands. It didn't matter if the ships were made of wood or metal or the slope was rather flat or a bit more steep. By centuries of experience the management was good and the side launch well prepared. The side launch often proved to be successful. Indeed it was a weekly returning event and the many experiences were passed on from one worker to the other.

However, nowadays the production of uniform ships is moving to cheap labor countries for obvious reasons. This movement threatens the continuation of Dutch shipyards. A number of shipyards have chosen to change their production to custom made ships, but this leads to other problems.

These days the side launch has become a rare occurrence in the Netherlands and workers with experience are often retired. The changed parameters are becoming a risk and management is getting more difficult. Shipyards are in need for a methodology that can predict the outcome of a side launch, such that ship builders can in advance alter the parameters of the launch if needed and again minimize the risk of a failed side launch.

Already in 1947 Ju. S. Jakovlev started with calculations of the side launch. In his work *Berekeningen en experimentele proeven van opdrijven, stabiliteit en tewaterlating* [10] he built up a fully three dimensional mathematical model for the side launch. The model was however too difficult to use in a program and do calculations with.

In 1971 Chr. M. van Hooren altered the computations of Jakovlev, which made the model somewhat easier. In his *ingenieursexamenopgave* [9] he presented results of his work. A few years earlier J. Versluis had done experiments with models of vessels [14] to learn how scaled models were able to predict the movement of real vessels. Van Hooren used this knowledge to do various model experiments. With the results of it he tested his computations.

Nowadays computers are far more capable of doing this kind of calculations and methods have evolved over the years. The hardest part by far was and is the computation of the free surface of the water together with its hydrodynamic force. For almost a decade now, the mathematical department of the *University of Groningen* is developing a program ComFlo, originally an idea of A. E. P. Veldman. It can efficiently and thoroughly compute the free surface and hydrodynamic force. A detailed description of ComFlo can be found in the PhD theses of G. Fekken [6] or J. Gerrits [7].

These three ingredients, the model of Jakovlev, the improvements and test results of Van Hooren and ComFlo of Veldman, form the basis of this study. Last year this resulted in a master thesis of P. de Jong [11]. Many topics in the current thesis show similarity with the work of De Jong. To be complete though, most subjects are also included in this thesis. However, more work needed to be done. The program is now able to perform two and three dimensional simulations. Arbitrary three dimensional ship designs may be used in the computation and also the quay can be chosen more freely. A model for the wind is implemented and the input is enlarged with some more parameters. The program has been made more robust by filtering out pressure peaks.

After this introduction, chapter two gives the mathematical model of the program and chapter three the numerical model. In chapter four the results are presented and chapter five contains the conclusions. In appendix A, the experimental model of Van Hooren is given and appendix B contains the coefficients of the embedded Runge-Kutta method. Finally figures belonging to chapter four are found in appendix C. If interested a user guide of the program is available at the department of mathematics of the *University of Groningen*.

This project is carried out by order of SasTech and sponsored by the Dutch organization Nederland Maritiem Land and supported by the Vereniging voor Nederlandse Scheepsbouw Industrie, MARIN and Dutch shipyards like Volharding, Damen and De Hoop.

Chapter 2

Mathematical model

The mathematical model in the work of Ju. S. Jakovlev [10] forms the foundation for the mathematical model used in this project. The modifications done by Chr. M. van Hooren [9], a two dimensional motion of the vessel on the quay, are included also. The mathematical model for the hydrodynamic force is however not that of Jakovlev or Van Hooren, but that of ComFlo; a fully three dimensional Navier-Stokes solver of the *University of Groningen*.

In the first section of this chapter the equations of motion of the vessel are derived.The second, third and fourth section further explain the normal force on the quay, the hydrodynamic force of the water and the aerodynamic force of the wind respectively.

2.1 Equations of motion

The coordinate origin is defined as the point at the edge of the quay of the yz-plane containing the center of gravity G. The x-coordinate direction is defined along this edge, the z-coordinate direction is defined going straight down and the y-coordinate direction going right, perpendicular to both other axis (see Figure 2.1). The ϕ-, θ- and ψ-direction are the rotations around the x-, y- and z-coordinate direction through G respectively. The forces working on a moving vessel during launch are:

- the gravitational force P working on the center of gravity G,
- the friction force W working on sleigh-bottom/slope-top,
- the normal force N working on sleigh-bottom/slope-top,
- the hydrodynamic force R working on the part of the vessel beneath the surface and

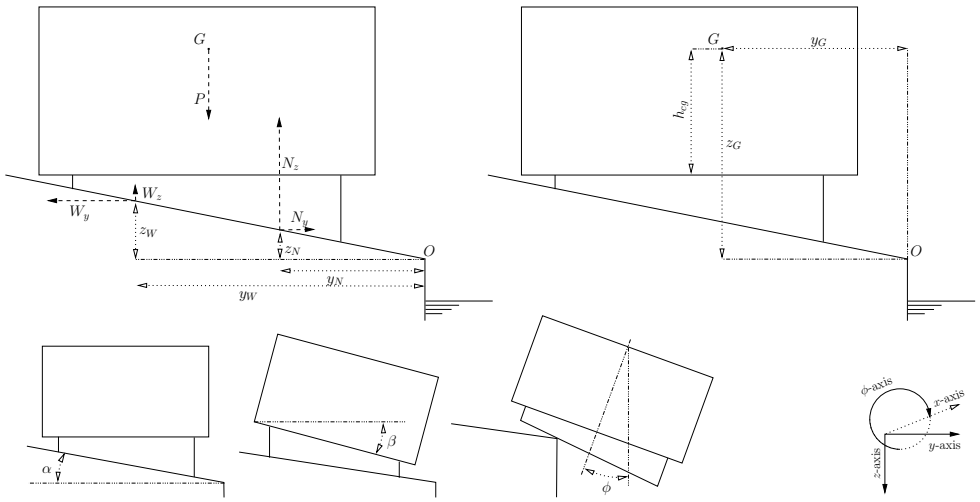

Figure 2.1: Top Left: Vessel with normal, friction and gravitational force; Top Right: Dimensions of the center of gravity of a vessel; Bottom Left: Three important angles of vessel and quay; Bottom Right: Most common coordinate directions.

- the aerodynamic force B working on the part of the the vessel above the surface.

Note that each force, say F, can be decomposed into forces in the three coordinate directions, F_x, F_y and F_z. Further define $G \equiv (x_G, y_G, z_G)$ with rotations $(\phi_G, \theta_G, \psi_G)$. The equations of motion now follow from Newton's second law of motion; $\boldsymbol{F}_{tot} = m\boldsymbol{a}$ for the linear case (with total force $\boldsymbol{F}_{tot}$, mass m and acceleration $\boldsymbol{a}$) and $\boldsymbol{M}_{tot} = \boldsymbol{I}\boldsymbol{\vartheta}$ for the angular case (with total torque $\boldsymbol{M}_{tot}$, moment of inertia $\boldsymbol{I}$ and angular acceleration $\boldsymbol{\vartheta}$):

$$
\begin{aligned}
m\ddot{x}_G &= P_x + W_x + N_x + R_x + B_x, && (2.1)\\
m\ddot{y}_G &= P_y + W_y + N_y + R_y + B_y, && (2.2)\\
m\ddot{z}_G &= P_z + W_z + N_z + R_z + B_z, && (2.3)\\
I_x\ddot{\phi}_G &= M_{W_x} + M_{N_x} + M_{R_x} + M_{B_x}, && (2.4)\\
I_y\ddot{\theta}_G &= M_{W_y} + M_{N_y} + M_{R_y} + M_{B_y}, && (2.5)\\
I_z\ddot{\psi}_G &= M_{W_z} + M_{N_z} + M_{R_z} + M_{B_z}. && (2.6)
\end{aligned}
$$

Because the direction of the gravitational force is parallel to the z-coordinate direction and the yz-plane containing G also contains the origin it follows:

$$P_x = P_y = 0, \tag{2.7}$$
$$P_z = P = mg. \tag{2.8}$$

During the launch as a relation between the normal force N and friction force W it is assumed $W = \mu_M\ N$. Here μ_M is dependent on the torque around the x-axis[1]. Because it is assumed the slope has no elevation nor descent in the x-coordinate direction there is no normal nor friction force in this direction. Abbreviating $\kappa_G = \phi_G + \alpha - \beta$ and using the relation between normal and friction force it follows (also see Figure 2.1):

$$N_x = 0, \tag{2.9}$$
$$N_y = N\sin(\kappa_G), \tag{2.10}$$
$$N_z = N\cos(\kappa_G), \tag{2.11}$$
$$W_x = 0, \tag{2.12}$$
$$W_y = \mu_M N\cos(\kappa_G), \tag{2.13}$$
$$W_z = \mu_M N\sin(\kappa_G). \tag{2.14}$$

Taking the direction of the force into account the equations of motion 2.1-2.6 can be rewritten to:

$$m\ddot{x}_G = B_x + R_x, \tag{2.15}$$
$$m\ddot{y}_G = -\mu_M N\cos(\kappa_G) + N\sin(\kappa_G) + B_y + R_y, \tag{2.16}$$
$$m\ddot{z}_G = P - \mu_M N\sin(\kappa_G) - N\cos(\kappa_G) + B_z + R_z, \tag{2.17}$$
$$I_x\ddot{\phi}_G = -\mu_M N\cos(\kappa_G)(z_G - z_W) + \mu_M N\sin(\kappa_G)(y_G - y_W) + N\sin(\kappa_G)(z_G - z_N) + N\cos(\kappa_G)(y_G - y_N) + M_{B_x} + M_{R_x}, \tag{2.18}$$
$$I_y\ddot{\theta}_G = \mu_M N\sin(\kappa_G)(x_G - x_W) + N\cos(\kappa_G)(x_G - x_N) + M_{B_y} + M_{R_y}, \tag{2.19}$$
$$I_z\ddot{\psi}_G = \mu_M N\cos(\kappa_G)(x_G - x_W) + N\sin(\kappa_G)(x_G - x_N) + M_{B_z} + M_{R_z}. \tag{2.20}$$

Here (x_N, y_N, z_N) and (x_W, y_W, z_W) are the points of application of the normal force N and friction force W respectively. They still have to be determined.

[1]It is assumed the vessel is subjected to a larger friction coefficient μ_M during the period of tilting.

There are three phases during the launch. In the first phase the vessel is located on the quay, in the second phase the vessel is tilting, but still has contact with the quay and in the third phase the vessel no longer has contact with the quay. Note that in any phase the vessel can hit the water. In comparison with Van Hooren, the movement on the quay before tilting is included (first phase), where Van Hooren excludes that part.

While in contact with the quay the motion is assumed to be fully two dimensional, although to achieve this, good management is needed. At SasTech necessary conditions to achieve a two dimensional launch have been studied[2].

Further simplifications are:

- To keep the motion simple during the first two phases assume the aerodynamic force has no influence then.
- The model does not allow the vessel to raise from the slope and thus no moment is required in the first phase.
- The normal and friction force N and W work in the same yz-plane as the center of gravity G and therefore $x_N = x_W = x_G$.
- In the second phase, when the vessel is tilting, the normal force N and friction force W are applied in the point of rotation, the origin, and therefore $y_N = y_W = z_N = z_W = 0$.

To shorten formulas define:

$$a = \sin(\kappa_G) - \mu_M \cos(\kappa_G), \tag{2.21}$$
$$b = \cos(\kappa_G) + \mu_M \sin(\kappa_G). \tag{2.22}$$

Now the equations of motion for the first phase become:

$$m\ddot{y}_G = Na + R_y, \tag{2.23}$$
$$m\ddot{z}_G = P - Nb + R_z, \tag{2.24}$$

which constitute two equations with unknowns $y_G(t)$ and $z_G(t)$. In the second phase the equations of motion are:

[2]For more information go to http://www.sastech.nl

$$
\begin{aligned}
m\ddot{y}_G &= Na + R_y, && (2.25)\\
m\ddot{z}_G &= P - Nb + R_z, && (2.26)\\
I_x\ddot{\phi}_G &= N(a\ z_G + b\ y_G) + M_{R_x}, && (2.27)
\end{aligned}
$$

which form three equations with unknowns $y_G(t)$, $z_G(t)$ and $\phi_G(t)$. In the third phase the equations of motion are:

$$
\begin{aligned}
m\ddot{x}_G &= R_x, && (2.28)\\
m\ddot{y}_G &= B_y + R_y, && (2.29)\\
m\ddot{z}_G &= P + B_z + R_z, && (2.30)\\
I_x\ddot{\phi}_G &= M_{B_x} + M_{R_x}, && (2.31)\\
I_y\ddot{\theta}_G &= M_{R_y}, && (2.32)\\
I_z\ddot{\psi}_G &= M_{R_z}, && (2.33)
\end{aligned}
$$

which constitute six equations with unknowns $x_G(t)$, $y_G(t)$, $z_G(t)$, $\phi_G(t)$, $\theta_G(t)$ and $\psi_G(t)$.

2.2 Normal force

If the vessel lies fully on the quay (first phase) $N = P\cos(\alpha) + R_z\cos(\alpha) - R_y\sin(\alpha)$. When the vessel is tilting (second phase) however, finding N is a bit more work. To find the normal force an extra relation is needed. This will be the constraint that says the sleigh's bottom makes contact with the slopes edge, as long as the sleigh is still above the slope.

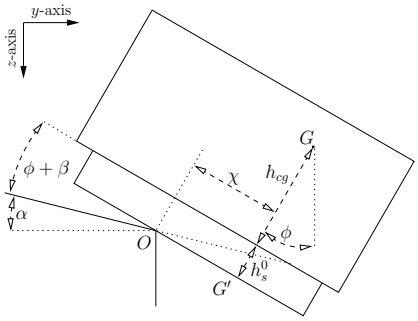

Figure 2.2: Vessel on quay rotated with an angle ϕ.

For the derivation first look at Figure 2.2. Note that the center of gravity is not necessarily at the center of the vessel. Further remember the movement on the quay is assumed to be fully two dimensional, so $x = 0$ is constant. The point G' is the projection of G on the sleigh bottom perpendicular to the vessel bottom. The distance between O and G' along the sleigh bottom is called χ. First again define $\omega = \alpha - \beta$ and again $\kappa_G = \phi_G + \alpha - \beta$. There are two angles important in the derivation:

$$\begin{aligned} \kappa_G &= \text{angle of the sleigh bottom w.r.t. the horizontal plane.} \\ \phi_G &= \text{angle of the vessel w.r.t. the vertical plane.} \end{aligned}$$

The position of G follows from $G = O + \vec{OG'} + \vec{G'G}$. The following holds (neglecting the x-coordinate temporarily):

$$\vec{OG'} = \big(\chi\cos(\kappa_G),\ \chi\sin(\kappa_G)\big) \tag{2.34}$$

$$\vec{G'G} = \big([h_{cg} + h_s^0]\sin(\phi_G),\ -[h_{cg} + h_s^0]\cos(\phi_G)\big) \tag{2.35}$$

and with this the coordinate of G becomes:

$$\begin{aligned} G \equiv (y_G, z_G) = \big(&\chi\cos(\kappa_G) + [h_{cg} + h_s^0]\sin(\phi_G), \\ &\chi\sin(\kappa_G) - [h_{cg} + h_s^0]\cos(\phi_G)\big) \end{aligned} \tag{2.36}$$

By now eliminating χ a relation between y_G, z_G and ϕ_G follows:

$$\begin{aligned} y_G\sin(\kappa_G) - z_G\cos(\kappa_G) = &[h_{cg} + h_s^0]\big(\sin(\phi_G)\sin(\kappa_G) \\ &+ \cos(\phi_G)\cos(\kappa_G)\big) \end{aligned} \tag{2.37}$$

Finally rearranging the terms in Equation 2.37 gives[3]:

$$z_G = y_G\tan(\kappa_G) - [h_{cg} + h_s^0]\frac{\cos(\omega)}{\cos(\kappa_G)} \tag{2.38}$$

[3]The extra relation between $y_G(t)$, $z_G(t)$ and $\phi_G(t)$ Van Hooren used in his project was not correct. Not taking the initial angle β in account he took as a relation:

$$z_G\cos(\phi_G) - y_G\tan(\phi_G + \alpha)\cos(\phi_G) = -[h_{cg} + h_s],$$

where the truthful formula is given by:

$$z_G\cos(\phi_G + \alpha) - y_G\sin(\phi_G + \alpha) = -[h_{cg} + h_s]\cos(\alpha).$$

For this constraint (Equation 2.38) to be useful, first it has to be differentiated twice with respect to the time t. This gives:

$$\ddot{z}_G = \ddot{y}_G f + \ddot{\phi}_G e + d \tag{2.39}$$

With e, d and f defined as:

$$\begin{aligned} d &= \frac{2\dot{y}_G\dot{\phi}_G\cos(\kappa_G) + 2y_G\ \dot{\phi}_G^2\sin(\kappa_G)}{\cos^3(\kappa_G)} \\ &+ [h_{cg} + h_s^0]\cos(\omega)\dot{\phi}_G^2\frac{\left(1+\sin^2(\kappa_G)\right)}{\cos^3(\kappa_G)} \qquad (2.40) \\ e &= \frac{y_G}{\cos^2(\kappa_G)} + [h_{cg} + h_s^0]\cos(\omega)\frac{\sin(\kappa_G)}{\cos^2(\kappa_G)} \qquad (2.41) \\ f &= \tan(\kappa_G) \qquad (2.42) \end{aligned}$$

With this and using Equations 2.25-2.27 the following holds for N:

$$N = \frac{(P + R_z) - (R_y f + M_{R_x}\frac{m\ e}{I_x} + m\ d)}{b + af + (a\ z_G + b\ y_G)\frac{m\ e}{I_x}}. \tag{2.43}$$

2.3 Hydrodynamic force

The hydrodynamic force is computed with ComFlo. It solves the Navier-Stokes equations for an incompressible and viscous fluid. This means the density of the fluid is constant and viscous effects are included in the computation. The Navier-Stokes equations consist of the conservation of mass (Eq. 2.44) and conservation of momentum (Eq. 2.45). They are given by:

$$\begin{aligned} \nabla\cdot\boldsymbol{u} &= 0, \qquad (2.44) \\ \frac{\partial\boldsymbol{u}}{\partial t} + (\boldsymbol{u}\cdot\nabla)\boldsymbol{u} &= -\frac{1}{\rho}p + (\nabla\cdot\nu\nabla)\boldsymbol{u} + \boldsymbol{F}. \qquad (2.45) \end{aligned}$$

Here $\boldsymbol{u}$ is the velocity vector, ρ is the density (which will be normalized to $\rho = 1$), p is the pressure, ν is the kinematic viscosity coefficient and $\boldsymbol{F}$ is an external force.

If the Navier-Stokes equations are solved a force $\boldsymbol{R}$ and torque $\boldsymbol{M_R}$ can be obtained. The force $\boldsymbol{R}$ is given by the integral of the pressure along the boundary Γ of the object Ω (here Ω is the vessel) and the torque $\boldsymbol{M_R}$ is the force $\boldsymbol{R}$ times the lever arm $\boldsymbol{r}$. Mathematically this means:

$$\boldsymbol{R} = \int_\Gamma p\boldsymbol{n}d\Gamma, \tag{2.46}$$

$$\boldsymbol{M_R} = \int_\Gamma p(\boldsymbol{r}\times\boldsymbol{n})d\Gamma. \tag{2.47}$$

Boundary conditions and free surface

To solve the Navier-Stokes equations boundary conditions are needed. The canal's sides and bottom are defined as free slip (Eq. 2.49) and are impermeable to water (Eq. 2.48). This also holds for the boundary of the vessel and therefore the solid boundary conditions are:

$$u_n = 0, \tag{2.48}$$

$$\frac{\partial u_t}{\partial \boldsymbol{n}} = 0. \tag{2.49}$$

Here $u_n = \boldsymbol{n}\cdot\boldsymbol{u}$ is the velocity normal to the wall, $u_t = \boldsymbol{u}\cdot\boldsymbol{t}$ is the tangential velocity, $\boldsymbol{n}$ is the normal direction and $\boldsymbol{t}$ is the tangential direction. The boundary conditions for the free surface are:

$$-p + 2\mu\frac{\partial u_n}{\partial \boldsymbol{n}} = -p_0 + 2\sigma H, \tag{2.50}$$

$$\mu\left(\frac{\partial u_n}{\partial \boldsymbol{t}} + \frac{\partial u_t}{\partial \boldsymbol{n}}\right) = 0, \tag{2.51}$$

where μ is the dynamic viscosity coefficient, p_0 is the atmospheric pressure, σ is the surface tension and $2H$ represents the total curvature of the surface. Further an equation is required for the displacement of the free surface. Suppose the position of this free surface is described by $s(\boldsymbol{x},t) = 0$, then the movement of the free surface is given by:

$$\frac{Ds}{Dt} = \frac{\partial s}{\partial t} + \boldsymbol{u}\cdot\nabla s = 0. \tag{2.52}$$

2.4 Aerodynamic force

For the aerodynamic force it is assumed that:

$$B = \frac{c_D\ \rho_a}{2}\ A\ V^2. \tag{2.53}$$

Here c_D is the drag coefficient[4], ρ_a the density of air, A the frontal area of

[4]A parachute has c_D-values around 1.40, a car around 0.40

the vessel in the direction opposite to the wind direction and V the velocity the wind strikes with.

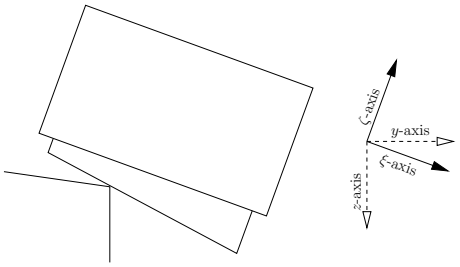

Figure 2.3: Vessel with ξ-axis and ζ-axis.

The difficulty in finding the force and torque is obtaining the frontal area. Hereto define two new coordinate directions, the ξ-direction and ζ-direction (see Fig. 2.3). They are equal to the y- and negative z-coordinate directions rotated with angle $\phi_G + \beta$.

Suppose V_B is the velocity of the wind. Then the velocity the wind hits the vessel with is given by:

$$v_\Delta = V_B \sin(\gamma_a)\cos(\gamma_b) - v, \tag{2.54}$$
$$w_\Delta = -V_B \sin(\gamma_a)\sin(\gamma_b) - w. \tag{2.55}$$

Here γ_a is the angle of the wind in the xy-plane with the lengthwise axis of the vessel and γ_b the angle of the wind with the horizontal plane (see Fig. 2.4), v_Δ is the velocity in y-direction and w_Δ is the velocity in z-direction.

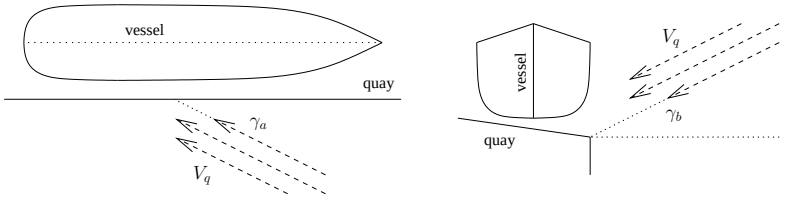

Figure 2.4: Wind inclination angles γ_a (left) and γ_b (right).

Now the following holds for the velocity in the ξ and ζ-direction:

$$V_\xi = v_\Delta \cos(\phi_G) + w_\Delta \sin(\phi_G), \tag{2.56}$$
$$V_\zeta = w_\Delta \cos(\phi_G) - v_\Delta \sin(\phi_G). \tag{2.57}$$

Computing the frontal area in the ξ and ζ-direction depends on different factors; the position of the edges, the angle of the vessel and the direction of the wind velocity. If you however know the areas A_ξ and A_ζ, computing the rest is a formality. Together with the center of gravity, also the lever arms a_ξ and a_ζ can be derived. As an illustration the case the wind blows from negative ξ and ζ directions and only the right chine is beneath water surface (so $\phi_G > 0$) is given:

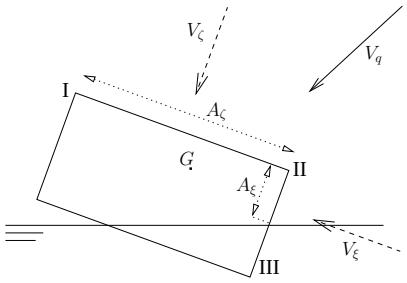

Figure 2.5: Vessel with one chine in the water and wind coming from the (upper) right.

Assume points **I**= (x_I, y_I, z_I), **II**= (x_{II}, y_{II}, z_{II}) and **III**= $(x_{III}, y_{III}, z_{III})$ are known and z_w is the z-coordinate of the free surface. The wind velocity V_q can be decomposed into a wind velocity V_ξ in the ξ-direction and a velocity V_ζ in the ζ-direction. In this case $V_\xi < 0$, $V_\zeta < 0$ and $\phi_G > 0$.
It is clear that A_ζ equals the width b_v times length l_v of the vessel. Further $A_\xi = l_v(z_{II} - z_w)/\cos(\phi_G)$. Now the lever arms $a_\zeta = (b_v/2 - y_G)$ and $a_\xi = \big((z_G - z_w) - (z_{II} - z_G)\big)$.
Like this, there are several cases depending on wind velocities V_ξ and V_ζ, the angle ϕ_G and the coordinates of the *edges*.

The aerodynamic force in the ξ- and ζ-coordinate direction now become:

$$B_\xi = \frac{c_D\ \rho_a}{2}\ A_\xi\ V_\xi^2, \tag{2.58}$$

$$B_\zeta = \frac{c_D\ \rho_a}{2}\ A_\zeta\ V_\zeta^2. \tag{2.59}$$

Going back to the y- and z-coordinate directions this means:

$$B_y = B_\zeta\ \sin(\phi_G) + B_\xi\ \cos(\phi_G), \tag{2.60}$$

$$B_z = -(B_\zeta\ \cos(\phi_G) - B_\xi\ \sin(\phi_G)), \tag{2.61}$$

$$M_{B_x} = B_\zeta\ a_\zeta + B_\xi\ a_\xi. \tag{2.62}$$

Chapter 3

Numerical model

The mathematical model of the previous chapter will be translated to a numerical model in this chapter. The numerical model is implemented in a program that performs the computer simulations of the launch and calculates the (free-surface) flow of the liquid. A large part of this chapter, namely section 3.2, is reproduced from the master thesis of G. Fekken [5].

In the first section the model used for computation of the motion of the vessel is treated. Here the position, rotation angle and (angular) velocity need to be derived. In the second section the working of ComFlo is explained, which solves the Navier-Stokes equations for free-surface flow and computes the hydrodynamic force and torque. A more extensive explanation of ComFlo is found in the PhD theses of Fekken [6] and Gerrits [7]. In the last section the interaction between the program and ComFlo is presented.

3.1 Ship motion

Suppose the position vector $\boldsymbol{x}_G$, the velocity vector $\boldsymbol{v}_G$ and the acceleration vector $\boldsymbol{a}_G$ are given by:

$$\begin{aligned} \boldsymbol{x}_G &= (x_G,\ y_G,\ z_G,\ \phi_G,\ \theta_G,\ \psi_G)^T, \\ \boldsymbol{v}_G \equiv \dot{\boldsymbol{x}}_G &= (\dot{x}_G,\ \dot{y}_G,\ \dot{z}_G,\ \dot{\phi}_G,\ \dot{\theta}_G,\ \dot{\psi}_G)^T, \\ \boldsymbol{a}_G \equiv \ddot{\boldsymbol{x}}_G &= (\ddot{x}_G,\ \ddot{y}_G,\ \ddot{z}_G,\ \ddot{\phi}_G,\ \ddot{\theta}_G,\ \ddot{\psi}_G)^T. \end{aligned}$$

Here x_G, y_G and z_G are the positions of the center of gravity and ϕ_G, θ_G and ψ_G are the angles around the three coordinate directions through the center of gravity.

The new (angular) velocity then follows by solving the ordinary differential equation $\dot{\boldsymbol{v}}_G = \boldsymbol{a}_G(t)$, where $\boldsymbol{a}_G$ is the acceleration vector, which gives

the (angular) acceleration on time t. The new positions and angles can be found by solving the ordinary differential equation $\dot{\boldsymbol{x}}_G = \boldsymbol{v}_G(t)$, where $\boldsymbol{v}_G(t)$ is the velocity vector, which gives the (angular) velocity on time t.

The solution methods used for finding positions, angles and (angular) velocities are however different from each other. The (angular) velocity is computed by a method, which uses an adjustable relaxation parameter. The position is found with a fourth-order Runge-Kutta method. The Runge-Kutta method is chosen because of its high order accuracy. Both methods will be explained in this section.

3.1.1 Cash-Karp Runge-Kutta

The program uses a Runge-Kutta method with a built-in method to control the truncation error to solve the ordinary differential equation for the position:

$$\dot{\boldsymbol{x}}_G = \boldsymbol{v}_G(t). \tag{3.1}$$

In order to control the size of the truncation error, first it must be estimated. In 1990 J.R.Cash and A.H.Karp published an article containing their so called Cash-Karp Runge-Kutta methods (see [4]). These methods compute the truncation error by comparing the computed answer with the result of an associated higher order Runge-Kutta formula. The two Runge-Kutta formulas are computed simultaneously and their difference is taken as an estimate of the truncation error.

In this project a fourth-order and fifth-order method are used. The fifth-order formula requires six evaluations of $\boldsymbol{v}_g$ per step. Consequently, Cash and Karp chose to use five evaluations of $\boldsymbol{v}_g$ for the fourth-order formula, rather then the usual four. This extra degree of freedom in choosing the fourth-order formula results in a smaller truncation error.

The Runge-Kutta formula uses coefficients $a_{i,j}$, b_i and c_i. Their values can be found in appendix B. Now in general the Runge-Kutta formula is given by:

$$(\boldsymbol{x}_G)_{n+1} = (\boldsymbol{x}_G)_n + b_1 k_1 + \ldots + b_m k_m. \tag{3.2}$$

Here k_i is:

$$
\begin{aligned}
k_1 &= dt\ f(t + c_1\ dt, y_n), \\
k_2 &= dt\ f(t + c_2\ dt, y_n + a_{2,1}\ k_1), \\
&\dots \\
k_m &= dt\ f(t + c_m\ dt, y_n + a_{m,1}\ k_1 + \ldots + a_{m,m-1}\ k_{m-1}),
\end{aligned}
$$

where here $f(t, \boldsymbol{x}) = \boldsymbol{v}_g(t)$. The iteration stops when the difference between the fourth- and fifth-order value of $(\boldsymbol{x}_G)_{n+1}$ is small enough.

Adaptive time step

In order to assess the accuracy of numerical integration and possibly adjust the step size to maintain the requested accuracy step doubling is employed. Remember a fifth order accuracy is obtained by Cash-Karp. Now the algorithm is as follows:

1. Take the step twice; once as a full step, leaping to $(\boldsymbol{x}_G)_{n+1}$ and then as two half steps, leaping to $(\boldsymbol{x}_G)^*_{n+1}$ with time step Δt.

2. Estimate the truncation error by $\Delta \boldsymbol{x}_G = (\boldsymbol{x}_G)^*_{n+1} - (\boldsymbol{x}_G)_{n+1} \approx O((\Delta t)^5)$.

3. Return $(\boldsymbol{x}_G)^*_{n+1}$ as an answer, because that is going to be the more accurate one. Since $\Delta \boldsymbol{x}_G \approx O((\Delta t)^5)$ and assuming that two different values of Δt are tried, the following holds:

$$
\frac{(\Delta \boldsymbol{x}_G)_0}{(\Delta \boldsymbol{x}_G)_1} = \left(\frac{(\Delta t)_0}{(\Delta t)_1} \right)^5 .
$$

   This yields the following formula for a step size

$$
(\Delta t)_0 = (\Delta t)_1 \left| \frac{(\Delta \boldsymbol{x}_G)_0}{(\Delta \boldsymbol{x}_G)_1} \right|^{1/5} . \tag{3.3}
$$

4. Let $(\Delta \boldsymbol{x}_G)_0$ be the requested accuracy. If $(\Delta \boldsymbol{x}_G)_0 < (\Delta \boldsymbol{x}_G)_1$ equation (3.3) tells us how much to reduce the step size when the failed step is repeated. Else, if $(\Delta \boldsymbol{x}_G)_0 > (\Delta \boldsymbol{x}_G)_1$, it tells how much it can be stretched in the next step.

3.1.2 Velocity solving method

To retrieve the velocity, the ordinary differential equation:

$$\dot{\boldsymbol{v}}_G = \boldsymbol{a}_G(t) \tag{3.4}$$

is solved. Here $\boldsymbol{a}_G = \left(\frac{(F_{tot})_x}{m}, \frac{(F_{tot})_y}{m}, \frac{(F_{tot})_z}{m}, \frac{(M_{tot})_x}{I_x}, \frac{(M_{tot})_y}{I_y}, \frac{(M_{tot})_z}{I_z}\right)^T$. Rewriting and discretizing equation (3.4) gives:

$$\frac{\boldsymbol{v}_G^{n+1} - \boldsymbol{v}_G^n}{dt} = \boldsymbol{a}_G^{n+1}. \tag{3.5}$$

and thus after rearranging the terms it would give:

$$\boldsymbol{v}_G^{n+1} = \boldsymbol{v}_G^n + dt\ \boldsymbol{a}_G^{n+1}. \tag{3.6}$$

Now after implementing a relaxation parameter ω the solving method becomes:

$$(\boldsymbol{v}_G^{n+1})_{k+1} = (1-\omega)\ (\boldsymbol{v}_G^{n+1})_k + \omega\ \left(\boldsymbol{v}_G^n + dt\ (\boldsymbol{a}_G^{n+1})_k\right). \tag{3.7}$$

The method iterates until the error $||(\boldsymbol{v}_G^{n+1})_{k+1} - (\boldsymbol{v}_G^{n+1})_k||$ is small enough. Initially ω is set equal 1, but if the velocity does not converge sufficiently ω becomes $\omega/2$ until a suitable ω is found. Than the iteration is continued until the error is small enough.

3.2 ComFlo

The program ComFlo solves the Navier-Stokes equations and retrieves the shape of the free-surface. Hereto a mesh is needed and the Navier-Stokes equations must be discretized in time and space. In this section these topics can be found and also the solution method of the pressure equation is given with the filter model and the time step stability control using the CFL-number.

3.2.1 Computational grid

In this study a Cartesian grid approach is used. The domain, containing vessel and quay, is covered with a rectangular grid with staggered variables; the pressure is determined in cell centers, the velocities at cell boundaries. The grid is structured and orthogonal[1] (see Fig 3.1). With this approach

[1]The cells are not necessarily squares. They may be stretched or shrunken in one or more directions.

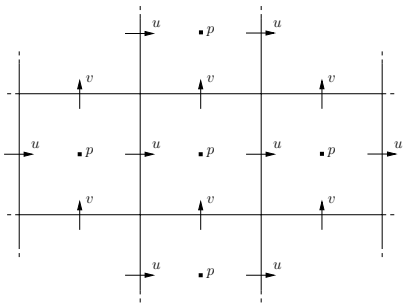

Figure 3.1: Left: Location of the pressure and velocity components.

neighbors are known immediately and it allows (moving) complex shaped geometries without a time consuming grid generation.

Apertures

Complex structures are covered with a Cartesian grid, thus cells with different characters originate. To be solved suitable each different cell character must be known and therefore a numerical method by edge and volume apertures is introduced. These edge and volume apertures are a measure for which part of the edge or volume is open to flow. They are divided in two classes (see Fig. 3.2):

1. volume apertures

   In every cell the aperture F_b defines the fraction where fluid is able to flow. The fluid aperture F_s defines the fraction of the cell which is occupied by fluid. Now $0 \leq F_s \leq F_b \leq 1$.

2. edge apertures

   The apertures A^x and A^y (and A^z) define the fraction of the cell faces that are open in x- and y-direction (and z-direction) respectively

Labels

Based on the aperture, the cells are given geometry labels for pressure and velocity that describe what kind of cell it is: a (**F**)low, a (**B**)oundary or an e(**X**)terior cell. To describe the free surface, the (**F**)low cells are underdivided in (E)mpty cells, (S)urface cells and (F)ull cells, using an indicator function. This distinction is expressed by free-surface labels that are determined every time step. The labels are determined by (see Fig. 3.2):

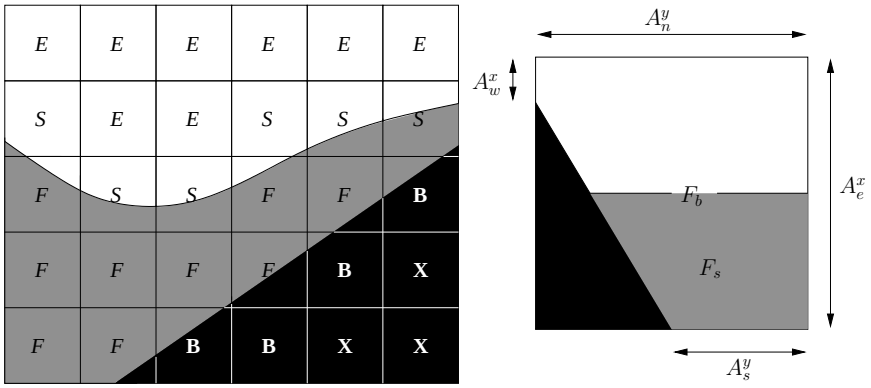

Figure 3.2: Left: Labeling geometry cells and free-surface cells. Right: Illustration of the definition of volume and edge apertures.

1. Geometry cell labels (time-independent)

   F-cells: cells with $F_b \geq \frac{1}{2}$
   B-cells: cells with $F_b < \frac{1}{2}$ adjacent to an **F**-cell
   X-cells: all remaining cells

2. Free-surface cell labels (time-dependent)

   E-cells: **F**-cells with $F_s = 0$
   S-cells: **F**-cells with $F_s \neq 0$ adjacent to an *E*-cell
   F-cells: all remaining **F**-cells

For the treatment of the velocity, the velocities between cells have to be labelled too. These velocity labels have, like the cell labels, two classes.

1. Geometry velocity labels

   These (time-independent) labels are a combination of the labels of the geometry cells where the velocities lie in between. The five possible combinations are **FF**, **FB**, **BB**, **BX** and **XX**.

2. Free-surface velocity labels

   These time-dependent labels are a combination of the labels of the free surface cells. The eight possible combinations are *FF*, *FS*, *SS*,*SE*, *EE*, *FB*, *SB* and *EB*.

Computing apertures and labels

Determining apertures and labels is an important part of the program, because it plays a crucial role in the discretization. Eventually the free surface will also be computed from these apertures and labels. At the boundary of a moving body extra care must be taken. Here apertures become time-dependent and the pressure is very sensitive to these aperture changes. Furthermore a necessary property is that the computation must be (almost) volume conservative, otherwise unphysical holes or pressure waves could appear in the fluid.

The procedure of finding the volume apertures is a kind of Marker-and-Cell method. Every cell is filled with a number of markers that are uniformly spaced in every cell. Each marker is the center of a virtual rectangular box. The edge apertures are found with a piecewise linear interface reconstruction (PLIC) method based on filling ratios in a cell and a normal at the surface. All labels are found using these apertures.

3.2.2 Discretization of Navier-Stokes

When all cells and velocities are labeled, the Navier-Stokes equations can be discretized in time and space. Hereto write them as:

$$\nabla \cdot \boldsymbol{u} = 0 \tag{3.8}$$

$$\frac{\partial \boldsymbol{u}}{\partial t} + \nabla p = \boldsymbol{R} \tag{3.9}$$

Here conservation of momentum is simplified with $\boldsymbol{R} = (\nabla \cdot \nu \nabla)\boldsymbol{u} - (\boldsymbol{u} \cdot \nabla)\boldsymbol{u} + \boldsymbol{F}$, containing all convective, diffusive and external forces and the density ρ is normalized to 1.

Time discretization

For the time discretization the explicit first order forward Euler method is used. The time discretized equations are:

$$\nabla \cdot \boldsymbol{u}^{n+1} = 0, \tag{3.10}$$

$$\frac{\boldsymbol{u}^{n+1} - \boldsymbol{u}^n}{\delta t} + \nabla p^{n+1} = \boldsymbol{R}^n. \tag{3.11}$$

Here n and $n+1$ denote the old and new time level respectively. Further δt is the time step, $\boldsymbol{u}^n$ is the velocity field and p^{n+1} is the pressure distribution. By choosing p at the new time level, the new velocity field from Equation 3.11 will be divergence free. Further $\boldsymbol{R}^n$ is the discretized version of $\boldsymbol{R}$.

Spatial discretization

The spatial discretization is based on the finite volume method, which makes use of conservation cells. In these cells both conservation of mass and momentum is required.

The equation for conservation of mass is applied in the center of the cell and a central discretization is used. The equation for conservation of momentum is applied in cell faces. In the discretization of $\boldsymbol{R}^n$, say $\boldsymbol{R}_h^n$, the diffusive terms are discretized centrally and for the convective terms both upwind and central discretization is possible[2].

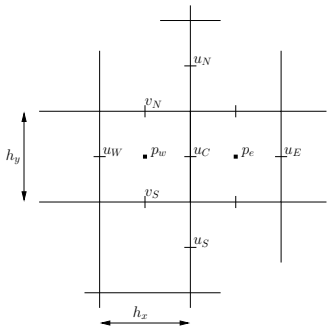

Figure 3.3: Conservation cell(s) for spatial discretization.

This results in the following Navier-Stokes equations. In the cell with center p_w the discretization of Equation 3.10 becomes:

$$\frac{u_C^{n+1} - u_W^{n+1}}{h_x} + \frac{v_N^{n+1} - v_S^{n+1}}{h_y} = 0 \quad (3.12)$$

The discretization of Equation 3.11 in point C becomes:

$$\frac{u_C^{n+1} - u_C^n}{\delta t} + \frac{p_e^{n+1} - p_w^{n+1}}{h_x} = R_h^n \quad (3.13)$$

Near the free surface

Near the free surface not only F-cells appear, but also S-cells and E-cells. The pressure p_F in the F-cells is determined with the Poisson equation (see the next section). The other two should be found differently. In E-cells the pressure is set to the atmospheric pressure p_0.
In S-cells the pressure is found with Equation (2.52) by neglecting the term $2\mu\frac{\partial u_n}{\partial n}$. Then $p_f = p_0 - 2\sigma H$. Now p_S is given by:

$$p_S = \eta p_f + (1-\eta)p_F \quad (3.14)$$

with $\eta = h/d$ (see Fig. 3.4).

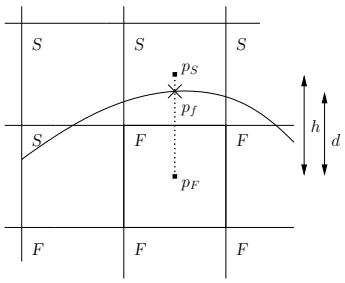

Figure 3.4: Pressure interpolation in S-cells.

[2]For wildly moving fluids mostly upwind discretizations are used because of stability reasons.

3.2.3 Pressure equation

To get the pressure p^{n+1} in F-cells the Poisson equation must be solved. This equation is obtained by substituting Equation 3.10 into Equation 3.11, which results in:

$$\Delta p^{n+1} = \nabla \cdot (\frac{\boldsymbol{u}^n}{\delta t} + \boldsymbol{R}^n). \tag{3.15}$$

Now let D_h denote the discrete divergence operator and G_h the discrete gradient operator. Further the divergence operator is divided in an operator on **F**-cells, D_h^F, and an operator on **B**-cells, D_h^B, so that $D_h = D_h^F + D_h^B$.

Use $\boldsymbol{u}^{n+1} = \boldsymbol{u}^n$ for the unknown velocities on the boundary at the new time level. Now the discretized equations are:

$$\begin{aligned} D_h^F \boldsymbol{u}^{n+1} &= -D_h^B \boldsymbol{u}^n, & (3.16)\\ \boldsymbol{u}^{n+1} &= \boldsymbol{u}^n - \delta t G_h p^{n+1} + \delta t \boldsymbol{R}_h^n, & (3.17) \end{aligned}$$

and the discretized Poisson equation for the pressure becomes:

$$D_h^F G_h p^{n+1} = D_h^B \frac{\boldsymbol{u}^n}{\delta t} + D_h^F (\frac{\boldsymbol{u}^n}{\delta t} + \boldsymbol{R}_h^n). \tag{3.18}$$

This Poisson equation is solved using SOR-iteration with an automatically adjusted relaxation parameter (i.e. a Gauss-Seidel method with over-relaxation, described by Botta and Ellenbroek [3]). Equation 3.18 can in general be written as:

$$C_p p_p + C_n p_n + C_s p_s + C_e p_e + C_w p_w + C_u p_u + C_d p_d = f_p. \tag{3.19}$$

The discrete operator $D_h^F G_h$ in equation 3.18 consists of a central coefficient C_p and coefficients of the six neighboring cells C_n, C_s, C_e, C_w, C_u and C_d. Near the free-surface and boundary some coefficients take special values or vanish. The right hand side is given by f_p.

The SOR-iteration can be written as:

$$\begin{aligned} (p_p^{n+1})_{k+1} &= (1-\omega)(p_p^{n+1})_k + \tfrac{\omega}{C_p}\big(f_p - C_n(p_n^{n+1})_k - C_e(p_e^{n+1})_k \\ &\quad - C_u(p_u^{n+1})_k - C_s(p_s^{n+1})_{k+1} - C_w(p_w^{n+1})_{k+1} - C_d(p_d^{n+1})_{k+1}\big). \end{aligned}$$

When the SOR-iteration has finished and the new pressure values are known, the new velocities can be computed using Equation 3.17.

Pressure filter

After the new pressure p^{n+1} is determined, there is the option to use a filter that smoothens the pressure[3]. The pressure peaks that need to be filtered last one time step. Therefore the filter keeps record of the two latest pressure values and the new value (i.e. p^{n-1},p^n and p^{n+1}) and returns the median for computation of hydrodynamic force and torque.

CFL-number

For stability it is useful to adjust the time step. A wildly moving fluid needs a smaller time step than when the fluid is moving calm. At the end of the time cycle, the time step will be adapted using the CFL-condition (Courant-Friedrichs-Lewy). The CFL-number is calculated here as:

$$CFL = \sum_{i,j,k} \left(\frac{|u_{ijk}|\delta t}{h_{x,i}} + \frac{|v_{ijk}|\delta t}{h_{y,j}} + \frac{|w_{ijk}|\delta t}{h_{z,k}}\right). \tag{3.20}$$

Here u_{ijk}, v_{ijk} and w_{ijk} are velocities of the cell i, j, k and $h_{x,i}$, $h_{y,j}$ and $h_{z,k}$ are the corresponding cell dimensions. Further δt is the time step.

The time step is now adjusted by bounding the CFL-number; if the computed CFL-number becomes too large the time step will be halved and if the computed CFL-number is small for ten successive time steps the time step will be doubled.

3.3 Coupling

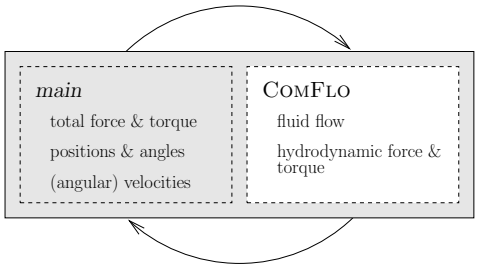

Figure 3.5: Order of computational steps. The *main* program is symbolized by the gray box. The white box (with dashed edges) represents the part of the program that originally was ComFlo.

[3]for more information about the filter's causes and effects see chapter 4.2

As said earlier the *main* program uses ComFlo for the computation of the hydrodynamic part. In fact the *main* program is a shell (or rind) around ComFlo and ComFlo has become more or less a large subroutine.

The *main* program contains subroutines that derive the motion of the vessel, thus subroutines to compute the total force and torque and for finding the (angular) velocities, positions and angles (see Figure 3.5). ComFlo Computes the fluid flow and the hydrodynamic force and torque.

Every time step first the hydrodynamic force and torque are computed. With it, the main program calculates the total force and torque. Now using the methods from section 3.1 the (angular) velocities[4], positions and angles are derived. In time the communication can schematicly be symbolized by:

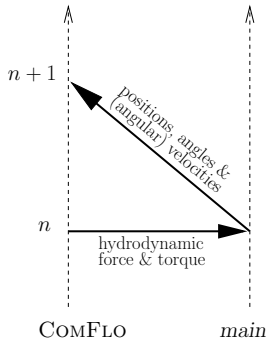

Figure 3.6: Time line of the *main* program and ComFlo including the communication between both.

The *main* program itself of course saves the old positions, angles and (angular) velocities of the vessel and also ComFlo keeps up the fluid flow.

[4]in fact the velocity is found simultaneously with the hydrodynamic force and torque (pressure) and thus the hydrodynamic force and torque can be called in several times in one time step.

Chapter 4

Results

To be useful the mathematical and numerical model derived in the previous chapters need validation. The simulations of the program are therefore compared with model experiments. These experiments were done by Chr. van Hooren [9] in 1978. For several launching cases he kept records of the position of the center of gravity and the rotation angle of the vessel around the lengthwise axis. The parameters of the cases of Van Hooren are described in appendix A.

For the validation here in the first section of this chapter a draft test is done, after which a grid refinement study is carried out in the second section. The third section analyzes the pressure filter and in the fourth section several experimental cases, described in Appendix A, are done. Some parameters of the launch are altered and the results are given in the fifth section. Finally a short parameter study is done in section six.

4.1 Draft test

The first test is a draft test. The draft of a vessel is already known at the design stage of a vessel and can also be computed with the Archimedes law. Because the draft of a vessel can be computed in advance, the accuracy and appropriate working of the program can be tested simply in this manner by comparing with the draft of the simulation.

Two tests have been done. The first test is two dimensional, the second test is three dimensional. In the tests a vessel is placed in the water with the center of gravity at zero water level. The vessel is therefore (typically) not in rest and it will heave over time to a stable situation.

According to the law of Archimedes in this stable situation the gravitational force $F_g = mg$ and the Archimedes force $F_A = \rho g \nabla$ cancel each other

(see Keuning and Bom [8]). From this the underwater volume ∇ and thus the draft can be computed. Remember however that the domain of the water is closed; there will be no in- or outflow. Due to the mass of the vessel, the water level changes when the vessel heaves in the water.

Two Dimensional

In the two dimensional case, all length scales are standardized to one. The water domain has dimensions $(l \times b \times h)$ $1.0 \times 2.0 \times 0.24\ m^3$ and the dimensions of the vessel are $(l \times b \times h)$ $1.0 \times 0.47 \times 0.228\ m^3$. The mass of the vessel is almost $27.2\ kg$ and the height of its center of gravity is $0.162\ m$.

When the vessel eventually lies in the water in rest, the water displacement is $27.2/999.63 \approx 0.027\ m^3$. According to the law of Archimedes, the draft should then be approximately $0.027/(1 \times 0.47) \approx 0.058\ m$. Caused by the initial placement of the vessel (the center of gravity at zero water level), the water level has dropped about $0.024\ m$ when the vessel reaches the stable situation. The center of gravity therefore must oscillate around $z_G = 0.162 - 0.058 - 0.024 = 0.080$.

Three Dimensional

In this case the water domain has dimensions $(l \times b \times h)$ $8.5 \times 2.0 \times 0.24\ m^3$ and the dimensions of the vessel are $(l \times b \times h)$ $1.76 \times 0.47 \times 0.228\ m^3$. The mass of the vessel is $47.8\ kg$ and the height of its center of gravity is still $0.162\ m$.

The water displacement of the vessel is $47.8/999.63 \approx 0.048\ m^3$. The draft of the vessel is $0.048/(1.76 \times 0.47) \approx 0.058\ m$. The drop of the water level is of course far less than in the two dimensional version. It should fall about $0.005\ m$. In stable position the height of the center of gravity thus lies at $0.162 - 0.058 - 0.005 = 0.099\ m$.

Result

As can be seen in Figure 4.1 in the two dimensional case the vertical position z_G oscillates around $z_G = 0.080\ m$ perfectly and also in the three dimensional case the vertical position z_G oscillates around the computed value nicely. It may be assumed our program works correct.

At open sea the heaving of the vessel would probably be more sinusoidal. Here the motion is a bit irregular. This again is caused by the closed domain where liquid can not escape. The water, heaving also, repeatedly but unregularly weakens or strengthens the motion of a vessel.

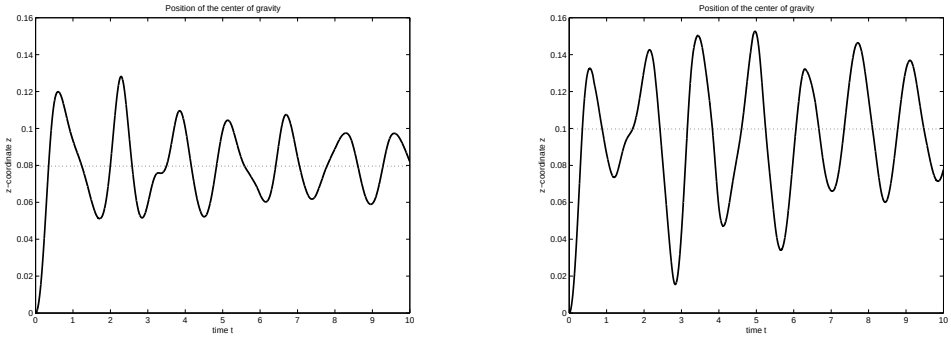

Figure 4.1: The vertical position z_G of the vessel in a draft test done with cell dimensions 0.013×0.011 m^2 ($2D$, left) and cell dimensions $0.28 \times 0.025 \times 0.022$ m^3 ($3D$, right).

Looking at the differences between the two and three dimensional model, it shows the deviation of the vertical position z_G in the two dimensional model is smaller. For a substantial part, this is caused by the bigger changes in the water level. The water level rises when the center of gravity drops and vice-versa and thus the amplitude is less in two dimensions.

This continuous and extreme changing water level in two dimensions is a big problem which corrupts similarity with real side launches. It affects the motion immediately. Therefore it can already be said that two dimensional simulations will not correspond with the experimental data of Van Hooren. In three dimensions there is a small raise too, however a small local raise in the beginning of the launch is probably seen in real launches too.

4.2 Spike test

In the early version of the program there were some troubles with large spikes in the pressure. They caused inaccuracies in the computation and slowed down the computation. The main cause of the spikes can be found as a consequence of labels, free surface or geometry, that change from one time step to the next, together with the divergence-free constraint. This divergence-free constraint makes the pressure very sensitive to irregularities in the flow. In many cases problems can be predicted and thus prevented, but, certainly with the involvement of a moving body, there is not always a simple solution[1].

The one time step pressure spikes are (primarily) due to the used method and not because of the physical laws. Because they are unphysical the spikes

[1]see section 2.4 of Fekken [6]

need to be removed. Hereto a filter was introduced (see chapter 3.2.3). The filter is supposed to remove single time step peaks in the pressure.

To evaluate the well-working of the filter, two tests are done. They are done according to case $2a$ of Van Hooren with cell dimensions $0.023 \times 0.022\ m^2$ for the first test and dimensions $0.011 \times 0.011\ m^2$ for the second test. In both tests the pressure is measured in a static point near bottom and quay over time. Note that the pressure is normalized by dividing by the atmospheric pressure p_0.

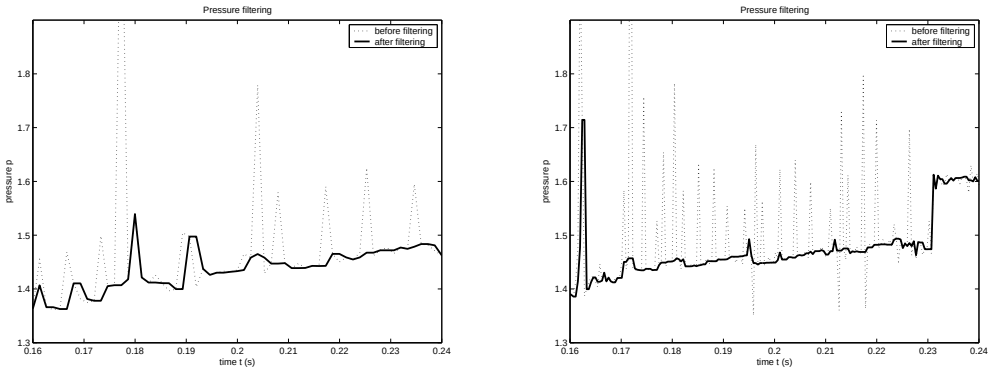

Figure 4.2: Spike test with cell dimensions $0.023 \times 0.022\ m^2$ (left) and $0.011 \times 0.011\ m^2$ (right).

The filter works as planned. Pressure peaks are filtered out and the pressure shows a less spiky curve. Not all pressure peaks are gone. Still some (smaller) peaks are seen. In the left figure a pressure peak is seen at $0.18s$ because there where two peaks directly after each other. In the right figure a peak is seen at $0.16s$ because the peak it filtered lasted more than one time step. Nevertheless the filtered model is certainly better than the unfiltered model.

4.3 Grid refinement

In this third test, the numerical model is validated. It is assumed a model converges to the mathematical model of the program if the grid is refined. The mathematical model can be represented by the experimental data so, if correct, the simulation data will approach the experimental data. With the results of the grid refinement study, also a grid size can be chosen to perform the remaining tests with. Note that references to figures containing a 'C' can be found in appendix C.

Two test sets are done with each three different grid sizes. The first test is two dimensional on a 80×30 grid, 160×60 grid and 240×90 grid. The second is three dimensional on a $30 \times 80 \times 30$ grid, $40 \times 100 \times 40$ grid and $50 \times 120 \times 50$ grid. Both tests use the parameters of case $2a$ of Van Hooren (see appendix A) and also both test sets use the pressure filter. To choose the grid for further simulations the computation time of the program is given also.

Two Dimensional

The simulation time for each experiment was:

computational grid	cell dimensions	computation time
80×30	$0.023 \times 0.022\ m^2$	$6\ min$
160×60	$0.011 \times 0.011\ m^2$	$1\ hour\ 16\ min$
240×90	$0.008 \times 0.007\ m^2$	terminated after $18\ hour$

See Figure C.1 of appendix C. The outcome of the simulation converges. There is hardly any significant difference between data from the 160×60 grid and the 240×90 grid. The experimental data is not approached well however, but that was expected in two dimensional simulations.

The simulation on the 240×90 grid wasn't even half way at the time the simulation was interrupted[2]. The computation times versus the accuracy suggest to use a 160×60 grid for the remaining two dimensional simulations. The improvements of a finer grid are not worth the effort.

Three Dimensional

The simulation time for each experiment was:

computational grid	cell dimensions	computation time
$30 \times 80 \times 30$	$0.28 \times 0.023 \times 0.022\ m^3$	$4\ hour\ 11\ min$
$40 \times 100 \times 40$	$0.213 \times 0.018 \times 0.016\ m^3$	$15\ hour\ 37\ min$
$50 \times 120 \times 50$	$0.17 \times 0.015 \times 0.013\ m^3$	$40\ hour\ 6\ min$

See Figure C.2. Although grid cells are larger than the two dimensional grid cells, graphs are still reasonably good and simulated data moves toward the measured data. Only the rotation angle is a bit disappointing.

[2]Large grid sizes still are a problem for the program. Computations on these fine grids now and than tend to slow down rapidly and therefore fail.

As could be expected the computation time is long with respect to the two dimensional simulations. The finest grid shows small improvements, but is also very expensive. Accuracy versus computation time proposes as a good grid size for the simulations $40 \times 100 \times 40$.

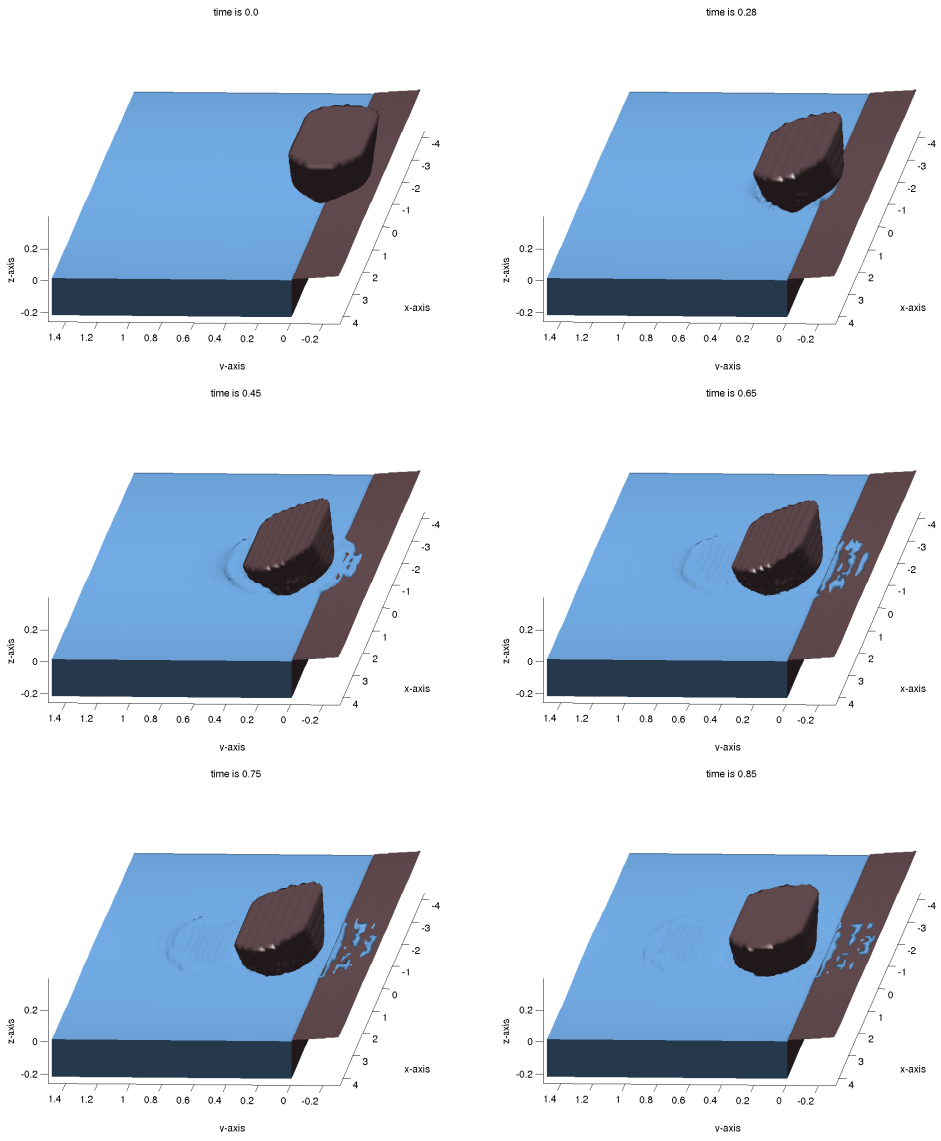

Figure 4.3: Snapshots of a simulation with a realistic hull.

4.4 Cases of Van Hooren

As said earlier Van Hooren did experiments in 1978 for several launch cases. Denote these cases as the *standard* test cases. Parameters of these cases are given in appendix A, where cases stated with an 'a' refer to experiments with a rectangular box and cases marked with a 'b' apply to experiments with a scaled model of the *Flynderborg*.

The thesis of De Jong [11] evaluates a two dimensional version of the program. He discusses the working by comparing $2D$ data to the experimental data of the standard 'a' tests with respect to the horizontal position y_G, the vertical position z_G, the rotation angle ϕ_G and also giving the position of both chines. Repeating those comparisons here is found not necessary and only a few of these simulations are done in the preceding section. Later (in section 4.5 and 4.6) some parameters of these standard test cases will be changed to investigate their influence. They will be compared with the simulations of this section, so that the effect of the changed parameter is highlighted explicitly.

Note that as from now all simulations use the filter, two dimensional simulations are computed with cell dimensions of approximately $0.11 \times 0.11\ m^2$ and in three dimensions of approximately $0.21 \times 0.018 \times 0.016\ m^3$. The figures of horizontal position (y-coordinate), vertical position (z-coordinate) and rotation angle (ϕ-coordinate) are given later in appendix C. Often the figure of the left chine (the shine at the quay side) is given though.

Two Dimensional

Many simulations have been done using the parameters of test case $2a$ (see appendix A), where only a single factor changes. This holds for all the tests with wind, the simulations with a moved center of gravity and simulations including one or more taluses. The simulations where the vessel has an initial angle have been done using the parameters of test case $8a$. The data of the two simulations, $2a$ and $8a$ are given in Figure C.3 and C.4 respectively.

Although some adjustments were done to the program, for instance the use of the pressure filter, the simulations correspond to the simulations of De Jong. In two dimensions the average rise of the water level is about 2.2 cm in comparison with the three dimensional cases. This rise is seen in the vertical position of the center of gravity too and the heaving of the water explains the height not following the experimental values of the center of gravity in the later. The water level rise also justifies the smaller first maximum angle in the rotation. Any further conclusions about the swinging motion are more or less unusable, due to this change in water surface height. Also note that

the model is scaled and 2.2 *cm* here is 55 *cm* in reality.

Three Dimensional

The above two test cases have been done three dimensional also. The difference in water elevation is not present here, because the simulation model is identical to the experimental model. Similar tests, cases 4*b* and 6*b* of Van Hooren, with a hull comparable with the hull of the *Flynderborg* are done here too. The shape data of the actual hull of the *Flynderborg* was not available anymore and the hull taken here was provided by SasTech and is a good estimate of it. The results of the four three dimensional simulations 2*a*, 8*a*, 4*b* and 6*b* are found in Figure C.5, C.6, C.7 and C.8 respectively. Note that these figures, besides the simulated and experimental results, also contain the data of Van Hooren's model for evaluation purposes later in section 4.6.

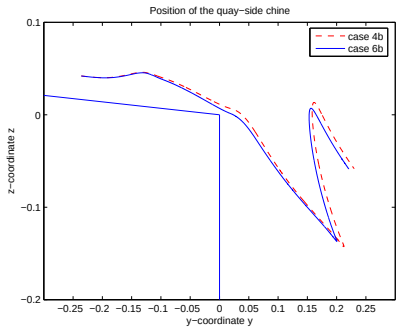

Figure 4.4: Position of the left chine for case 4*b* and 6*b*.

Cases 2*a* and 8*a* show good resemblance with the simulations. Only the horizontal position y_G in case 8*a* is poor, but it is corresponding with the simulation of Van Hooren. The rotation angle ϕ_G is overall better than in Van Hooren's simulation. The second maximum angle (back-swing) is just a little over the experimental value, but the first and third maximum angle differ about 0.1 *rad*. In comparison with the two dimensional counterpart, the three dimensional cases are better, mainly because of the better vertical positions of the center of gravity. Here the change in water level is very little and the draft now reaches its experimental value well.

The horizontal and vertical position of cases 4*b* and 6*b* show fairly good resemblance with the positions in the experiments. The rotation angle ϕ_G however has little similarity with the provided experimental data. Maximum values are different and the *period* is less. It is possible the difference between the used hull and the hull of the *Flynderborg* has a part in the difference of data and simulation. However again data of Van Hooren's simulation and

the present simulation are alike. Illustrative for the motion the path of the quay-side chine is given in Figure 4.4.

4.5 Variations to Van Hooren

Sometimes the conditions of the launch, unintended or on purpose, can change. It is therefore convenient to be able to compute such conditions in advance. Hereto a few common changes of a side launch are incorporated in the program. The integrated options are:

- First of all, it is not seldom to place ballast tanks on the vessel to change the position of the center of gravity. A center of gravity more on the quay side of the vessel is sometimes wanted. The vessel then has contact with the quay longer and thus rotates later and further away from the quay.
- Further, nowadays the side launch is sometimes performed with a so-called see-saw. Here the sliding starts with a heeling angle equal to the berth angle (i.e. $\phi_G > 0$), where normally the vessel starts with no angle (i.e. $\phi_G = 0$).
- Often the quay is not rectangular, but has a talus beneath the surface. A talus under water reduces the pressure there, which is highest in corners. Besides that a talus and/or slope could diminish the reflected wave and thus its influence on the motion.
- Finally, on the launch platform a wind could blow. If the wind is strong and the direction is opposite to the velocity of the vessel a critical situation could arise where the vessel is blown towards the quay.

Although the two dimensional simulations are not entirely satisfying, tests are done in two dimensions. The only interest is the change a parameter causes and this is supposed sufficiently alike in two versus three dimensions.

Moved center of gravity

Two cases have been tested and compared with case $2a$. In the first test case the center of gravity is moved with 5% of the total width, in the second test case with 10%. The advantage of the moved center of gravity is that the tilting starts later and thus the vessel plunges into the water further away from the quay. The risk of the vessel hitting the quay during its swinging motion is less, although the second maximum angle of ϕ_G is larger.

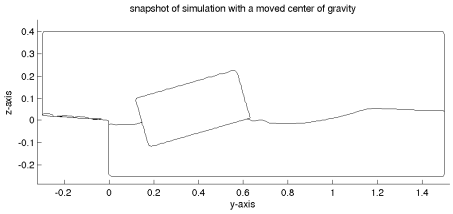

Figure 4.5: Position of vessel in the water when $JG = -0.047$ (10 % of total width).

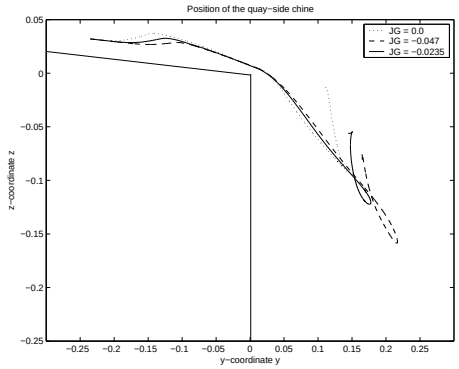

Figure 4.6: Position of the left chine of the vessel.

In Figure C.13, taking into account the 5% or 10% change in the horizontal position y_G, the coordinates stay the same. The vertical position z_G is more steady going to its minimum, but this minimum is less. The deeper position is caused by the angle the vessel has in the water (see Fig. 4.5). The angle of the vessel differs a lot in the 5% and 10% case. The stable angle is respectively about 0.15 rad and 0.25 rad less than a stable angle normally is (zero degrees).

To illustrate the movement of the chine on the quay side, its position is derived from y_G, z_G and ϕ_G and given in Figure 4.6. It is indeed further away from the quay if the center of gravity is more towards the quay, although the effect is very small.

Initial angle

Two tests have been done and compared with case 8a. In the first test the initial angle β of the vessel is 0.07 rad, just as the quay is, in the second the angle is 0.14 rad (see figure 4.7).

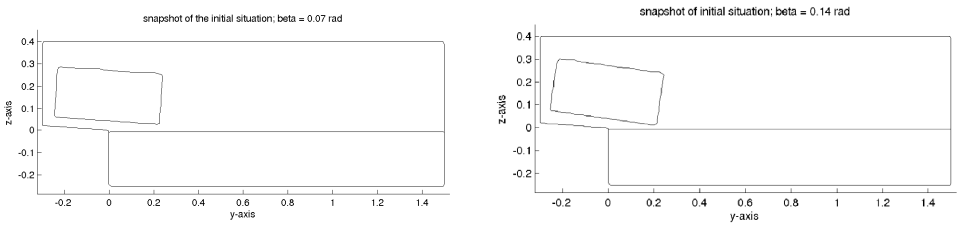

Figure 4.7: Snapshot of the initial situation for $\beta = 0.07$ rad (left) and $\beta = 0.14$ rad (right).

It should be mentioned that the velocity on the quay was constant during the simulation and equal to the velocity in the case there was no initial angle. In the see-saw launching method the velocity with which the vessel hits the water goes up if the sliding angle does. That would change the positions of the center of gravity. With the present constant velocity no great changes in the position are presumed and only the initial angle will be seen, but the angle ϕ_G is bound to adept to an angle of a normal launch over time.

Indeed, looking at Figure C.12 the horizontal and vertical positions y_G and z_G stay as good as the same. The rotation ϕ_G starts with an angle of 0.07 *rad* and 0.14 *rad* respectively, but this larger angle reduces over time to the stable value of 0.0 *rad*. Also the path of the quay-side chine (see Fig. 4.8) becomes similar after a period of time.

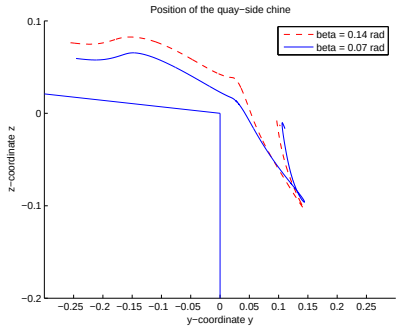

Figure 4.8: Position of the left chine for different initial angles.

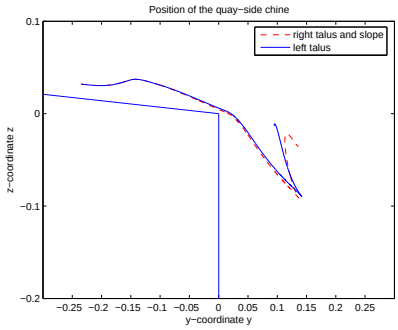

Figure 4.9: Position of the left chine for different quays.

Taluses

Two simulations have been done to test the influence of one or more taluses (see Fig. 4.10). In the first test a talus is placed at the side of the launch beneath the surface. The most important outcome of the talus should be expected when the reflected wave reflects again. This occurs only later in the simulation and thus not much change is anticipated now. In the other test the opposite side contains a talus and a slope. The reduced returning wave of the water should result in a position further away from the left quay and a vessel heaving less.

The results are presented in Figure C.10, Figure C.11. In the first test the position of the center of gravity indeed hardly changes and also the rotation stays the same. In the second test the position changes as soon as the returning wave could normally be expected, but the rotation again stays

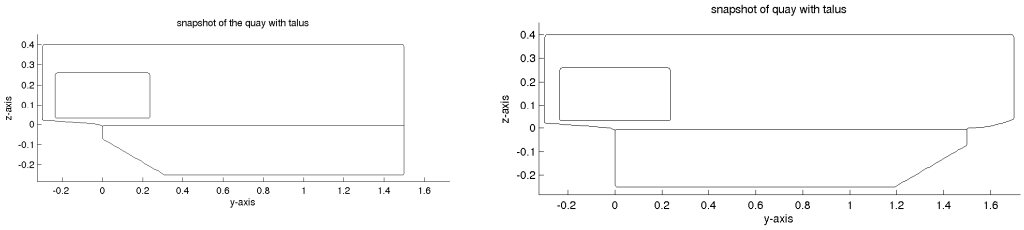

Figure 4.10: Snapshot of the quay in the first (left) and second (right) test.

the same in the simulation. In Figure 4.9 it is seen that the position of the chine comes further now the returning wave is less. The first part of the path is alike.

Wind

Three tests have been done including a wind model. It will be compared with the standard test case $2a$. First the wind velocity will be set to 0 m/s to just look at the effect of the aerodynamic force, after which the wind velocity is set to 16 m/s which is equal to the Beaufort scale 7. Also a test is done with the wind velocity set to 26 m/s, which is comparable with the Beaufort scale 10. In all tests the drag coefficient c_D is taken as $c_D = 1$. Note that the wind only influences the movement if the vessel is loose from the quay[3]; at $t = 0.51$. All three test cases use a headwind.

Due to the wind, the vessel is expected to reach a position less far from the quay. On the other hand the vertical position of the center of gravity probably won't change much. A small shift in the overall rotation angle ϕ_G can be expected too by the wind. For instance in a headwind the positive angle becomes smaller and the negative angle larger as the wind velocity increases.

Now look at Figure C.9. The consequences are minimal when the wind velocity is set to 0 m/s. In fact the *'no wind'*-graphs are not distinguishable from the *'0 m/s'*-graphs. Indeed the horizontal position y_G is closer to the quay as the wind velocity goes up. With that increase the rotation angle ϕ_G becomes less positive and more negative. Also the vessel hits the quay again when the velocity is set to 26 m/s and therefore fails. This can probably be expected with a Beaufort scale 10.

[3]To monitor the consequences of the aerodynamic force, the simulations are done over a longer period of time.

4.6 Additional tests

The figures of chapter 4, given in appendix C, show a significant change in the rotation ϕ_G, where the positions y_G and z_G are still fair. The simulations of Van Hooren show a similar change in position and rotation (see Figure C.3 to C.8). In his numerical model the new positions and velocities are determined with a simple Euler method though and the hydrodynamic force and torque are estimated with another method also, i.e. with the formulas:

$$\begin{aligned} R_y &= y''_G\, a_1 + \phi''_G\, b_1 + d_1 \\ R_z &= z''_G\, a_2 + \phi''_G\, b_2 + d_2 \\ M_{R_x} &= \phi''_G\, a_3 + y''_G\, b_3 + z''_G\, c_3 + d_3 \end{aligned}$$

where the coefficients a_1, a_2, ..., d_3 are given by a mixture of hydrodynamic mass, damping coefficients, positions and velocities of the vessel and its hull shape. The model completely neglects influences of shallow water, taluses and quay.

Because of the similar results and the different numerical method, it may be assumed the changes in position and rotation (between simulation and experiment) are not caused by the numerical model here. Assuming nothing is forgotten in the mathematical model, that is also not the source of the difference. To determine the role of the choice of the parameters in the discrepancy, two of them are tested here explicitly; the friction coefficient while tilting and the moment of inertia. Both are supposed to mainly affect the rotation.

Friction coefficient

In the test cases of Van Hooren the vessel was launched with a transporter-band with on the edge a cylinder. When the vessel was tilting it rested on this cylinder, which had a friction coefficient μ_M. Although this friction coefficient μ_M was assumed to be zero, Van Hooren searched for another value to fit the real value of μ_M better. Here three different values for the friction coefficient are tested also, namely $\mu_M = 0.0$, $\mu_M = 0.07$ and $\mu_M = 0.14$.

See Figure C.14. The inclusion of the friction during the rotation seems to slow the vessel down a bit. Where vertical position z_G is the same, the horizontal position y_G becomes less as μ_M increases. The first maximum angle is smaller and preserved over a longer period of time for larger values of μ_M. After the vessel is loose from the quay, the angle is alike with a shifted period. Looking at the path of the chine (Fig. 4.11) there is not much change in its path.

When μ_M equals 0.07 the simulated data seem to fit best to the experimental data. The error in the position is more or less equal, but the rotation has the better likeness in this case. The value $\mu_M = 0.07$ is the same value as Van Hooren found to fit the best. The simulation is however done two dimensional, where the results in general are less than in three dimensions. It seems though, the simulations can benefit from a well chosen friction coefficient μ_M.

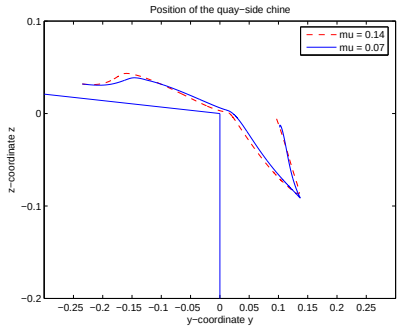

Figure 4.11: Position of the left chine for different values of μ_M.

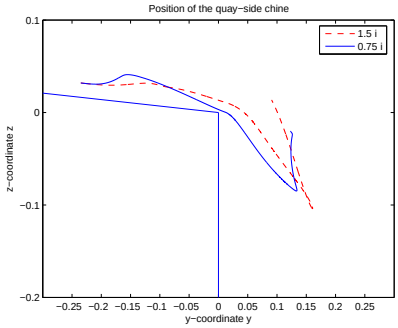

Figure 4.12: Position of the left chine for different values of the moment of inertia I.

Radius of inertia

Another value important to the rotation is the moment of inertia $\boldsymbol{I}$, which is used in the angular version of Newton's second law; $\boldsymbol{M} = \boldsymbol{I\vartheta}$ and thus controls the rotation (also see chapter 2.1). The moment of inertia I is a very important parameter in a side launch. Its value can be determined from the radius of inertia i by using the formula $I = i^2 m$, where m is the mass of the object. The radius of inertia describes the way in which the mass of a cross-section is distributed.

The user provides the parameter i. In the figures until now the angle ϕ_G shows overshoot as well as under-run and thus maybe the radius should be chosen different. Hereto a simulation is done for 75% and 150% of the normal value of i.

See Figure C.15. The position of course shows great similarity with the different radii. The rotation however changes. If the radius of inertia is less, the second and third maximum angles are less also and with a larger radius they are bigger. The value of the first maximum angle is not very different, but only the steepness and time at which this angle is reached change. The

larger radius has a longer *period* and is more steep. The path of the chine is more wild for a larger radius (see Figure 4.12).

The simulation again was two dimensional and in that case the given value has the best results. However in three dimensions the (second and third) maximum angle of ϕ_G is too large and the period is a bit too long. This could suggest a slightly shorter radius of inertia is better. Such a change in cases with the *Flynderborg* has a positive effect on the maximum angles too, but on the contrary probably makes things worse for the period. The period is already too short and thus a shorter radius of inertia reduces the period even more.

Chapter 5

Conclusions

In the following section first the results of chapter four are repeated globally and a judgement of it is given. After that the shortcomings and general inaccuracies of the simulating program are given. The next section couples these imperfections with the errors still made in the program and after that the last section contains some remarks on improving the program.

5.1 Results

The goal of the project was to create and validate a program that could predict the path of the side launch of a vessel. In the first project, done by P. de Jong, the two dimensional model was created, tested and validated and a three dimensional model was made and tested, but not validated.

This project continued where the first project ended. Irregularities in the mathematical model have been polished away. Some incorrect formulations of the normal force were rectified. Also, in comparison with the first project, the equations of motion were reduced to two equations in the first phase, because there was assumed to be no rotation there yet. In the third phase the equations were extended to six degrees of freedom, which is fully three dimensional.

In the numerical process a filter was introduced to reduce pressure spikes. As seen in the previous chapter, the filter works as planned. The program indeed proves to be more robust by applying the filter. Even though the computation overall takes a bit more time, the pressure iteration almost always converges. It is assumed the filtered value is far better than the large spikes it replaces. From the spikes you can be positive they are wrong and the filtered value lies within the expectation of values, which can not be *far* from previous values.

Further the program needed validation for three dimensional simulations. Hereto the program has been made able to read in an arbitrary three dimensional hull and do computations with it (see page 32). The $3D$ simulations show two major differences that need to be cleared up. First of all the occasional extreme difference in position in the y-direction, which is seen in some simulations. Secondly the rotation that does not follow the rotation of the experiment. For the simulations with a realistic hull this rotation also misses a good period of the swinging motion. Note that both effects are seen in the research of Van Hooren too.

Other features that were added are the quay that may contain several taluses, the vessel that can be rotated before starting the simulation and its center of gravity moved as done when ballast tanks are used. Also a wind model was added to the program to calculate the aerodynamic force. All features have been validated in the previous chapter. No unexpected and strange effects were seen comparing with simulations of normal[1] test cases.

5.2 Causes for errors

Due to the mathematical, numerical and experimental model the program has some shortcomings that can cause differences with the experimental data. The major deficiencies are:

I. *The assumptions made in section 2.1.*
In the derivation of the equations of motion some assumptions are done that aren't entirely correct. For instance the vessel practically never is launched perfectly in a two dimensional motion. Wind blows not only in the third phasem, but also during the first two phases and the friction force W can probably be computed more accurate.

II. *Other simplifying assumptions.*
For instance the experimental model of Van Hooren neglects the influence of equipment of the ship like the presents of a propeller or rudder. Also the shape of the quay is idealized; shapes of canal and slope are probably more curved and the canal consists of spongy mud on the bottom. Further there is always a self-induced aerodynamic force, which was neglected. Some of these options are implementable, but were not included in the computations.

III. *Parameters that are taken wrong in the calculations.*
As seen in chapter 4.6 the simulations are better when the friction coef-

[1] simulations of Van Hooren's standard test cases as stated in appendix A

ficient and/or the radius of inertia are taken different, in other words it is not unlikely that these parameters are chosen wrong. Also other parameters could be wrong, for instance the (hydro)dynamic coefficients like the density were chosen without knowing their real value.

IV. *The presence of systematic and random measuring errors.*
In his thesis Van Hooren spoke of the equipment having a measuring error. The instrument that measured the angles had an accuracy from about 0.05 rad. Also, in some test cases, the device showed a shift in the zero point after fanatical movement. Errors made in the rotation ϕ_G vary from -0.1 rad to 0.1 rad.

V. *Errors as a result of the numerical solving method.*
The method makes an $O(dt)$ and $O(d\boldsymbol{x})$ error in its computations and the pressure still introduces an error. The $O(dt)$ and $O(d\boldsymbol{x})$ error can of course be made smaller by grid refinement and smaller step sizes. In spite of the filter, the pressure contains spikes (although fewer and smaller) which influence the motion.

The first three causes are relatively small and the last two causes are probably the explanation for most errors. Anyhow, if one small error is made in position, angle or (angular) velocity of the vessel and the vessel is placed in a slightly different position with slightly different velocities, it influences the hole path.

5.3 Final discussion

The two dimensional simulations were found not appropriate for finding the path of the vessel. The change in water level disturbs the motion too much. In- and outflow conditions are needed at the beginning and end of the canal. Widening the canal is not an option, because that would make the reflecting wave go away.

As said the three dimensional model needs validation. The observed problems are given and discussed here. Although the actual cause is not clear, it is assumed that the fault can be found in one of the shortcomings of the previous section.

- The occasional extreme difference in the horizontal position (y_G):

  The difference in the position originates around $t = 0.5$. This is the moment the vessel is loose from the quay and thus the motion depends

fully on the hydrodynamic forces. Here a larger rotation angle ϕ_G, because of the larger friction in the y-direction, results in a smaller horizontal position (y_G-coordinate). The greater deceleration leads to bigger angle variations (larger pressures and thus forces) and so on. Although the difference in the horizontal positions were not large in the tests of the moment of inertia (where angles do vary), these kind of errors are probably the cause here.

- The rotation that does not follow the rotation of the experiment:

  The above problem is one of the causes here too. However the rotation could also benefit from changes in some of the parameters (III.). In chapter 4.6 it is already shown that if the moment of inertia and the friction coefficient are chosen different, it could profit the resemblance between simulation and experiment. There is a possibility if other parameters are changed a bit, they have a positive effect also. Further the measurement errors (IV.) are relatively large in the rotation angle ϕ, about 10% of the length of the interval. This explaines a part of the difference between the experimental rotation angle and the simulated angle.

- The even worse rotation in simulations with a realistic hull:

  In addition to the causes given for differences with the rectangular three dimensional hull, the wrongly chosen parameters (III.) are probably the main reason of the even worse rotation angle ϕ_G. The exact shape of the hull of the *Flynderborg* is not known and is not available anymore. The given hull was just a good guess of what it most likely would have been. Besides that Van Hooren also had poorer results in his simulations with realistic hull shapes.

The equations of motion of the vessel and formulas for the different forces have been checked several times by several people. Computations of the different forces is assumed to be correct (for instance the testing of ComFlo is done several years now and therefore it is hard to believe the free-surface and the hydrodynamic force are computed entirely wrong). Simulations with the side launch of a vessel are done extensively also and differences with the experimental data are often seen with Van Hooren too. Combining all, it becomes hard to believe computations are wrong and thus it is not unlikely

the mistake lies somewhere else. The given parameters are one of them, but measuring errors in the experiments are thinkable too. It is regrettable only one set of experiments is done and new data is therefore desirable.

The goal of the project was to create and validate a program that could predict the path of the vessel. In his conclusions of the two dimensional program De Jong was convinced the program would work after numerical problems (rapidly increasing velocities at vessel boundaries and pressure spikes) were solved. Also Van Hooren is positive about his program and the capabilities it has, but does express the need to include the influences of canal bottom and sides in the calculation of the hydrodynamic force.

With the validation done with the given data, it can be said here the program is not yet good enough to predict the path of the vessel accurately. It is however a good handhold for determining the major risks; slamming back against the quay and hitting the canal bottom. With an accurate vertical position (z_G), a lesser horizontal position (y_G) and a bigger second maximum rotation angle (ϕ_G) the risk of one of these events is only greater and thus if the simulation goes well, the actual launch will most certainly be good. For an accurate path however, the program still needs improvements.

5.4 Remarks for improvements

Finally there are some features that could improve the program even more. They are:

A. *Additional options*

- The option not to have a constant velocity on the slope, but one determined by total force and torque[2] and the option to have wind influnece that motion on the slope, where it now only works if the vessel lies in the water[2].
- The option to have in- and outflow in your domain at the front and end of the canal. It overcomes problems with changing water levels in namely $2D$ simulations. In three dimensional simulations making the quay long in the x-direction can help also, but this reduces the accuracy or needs more grid cells in that direction.

B. *Usability options*

[2]This option was not available during the validation, but in the meantime has been implemented.

- The input mechanism is very extensive and many options are never used or are more or less double. This should be made to one input file[2].
- The three dimensional simulations need an extra preprocessing step in which a three dimensional geometry is made. This is easier in one program, which does this step automatically[2].
- The inclusion of a quick-reference manual is probably handy, although a more extensive manual is available.

C. *Other improvements*

- At the moment fine grids are still hard to work with and three dimensional simulations tend to fail now and then. In other projects done with ComFlo it seems using *double precision* may offer a solutions.
- In his work on ComFlo and the interaction with moving objects Fekken says his model, which is also our model, for determining the velocity is rather simple. Implementation of a more robust and faster method would therefore be an interesting option (see chapter 2.5 of Fekken [6]).
- The position is determined using a constant velocity during each time step, although the velocity at the new time level is already known. The accuracy can probably benefit from this knowledge and is therefore worth looking at.

Appendix A

Experimental model

The setup of the model experiments from Van Hooren consisted of a scaled canal, slope and vessel with scaling 1:25. The canal was modeled by a rectangular tank with, in vertical direction, adjustable bottom. The slope was modeled using a transporter belt which allowed a constant velocity and prevented friction on it. Two vessels were used, the first was a box, the second a scaled model of a real ship; the *Flynderborg*.
Experiments done with the box are referred to with the letter 'a' and experiments with the *Flynderborg* with the letter 'b'. The parameters from the vessel of the experimental model standard (experiment $2a/2b$) are given by (see Figure A.1):

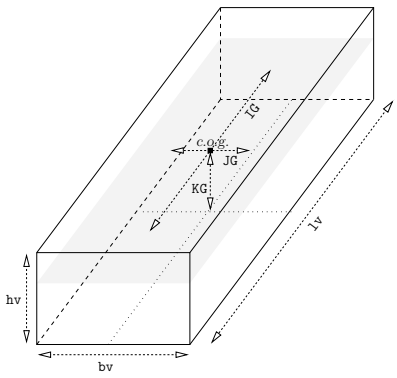

Figure A.1: Dimensions of the box-shaped vessel.

	description	symbol	value ($2a$)	value ($2b$)
vessel	length of vessel	lv	1.76 m	2.85 m
	width of vessel	bv	0.47 m	0.472 m
	height of vessel	hv	0.228 m	0.228 m
	relative x-position of G	IG	0.0 m	0.0 m
	relative y-position of G	JG	0.0 m	0.0 m
	relative z-position of G	KG	0.162 m	0.164 m
	mass of vessel	m	47.8 kg	48.8 kg
	x-radius of gyration	ix	0.170 m	0.191 m

	description	symbol	value ($2a$)	value ($2b$)
sleigh	width of sleigh	bs	0.47 m	0.472 m
	height of sleigh	hs	0.32 m	0.32 m
initial values	y-position	Y0	0.0 m	0.0 m
	z-position	Z0	0.194 m	0.196 m
	ϕ-angle	beta	0.0 rad	0.0 rad
	abs. velocity	V	0.6 m/s	0.6 m/s

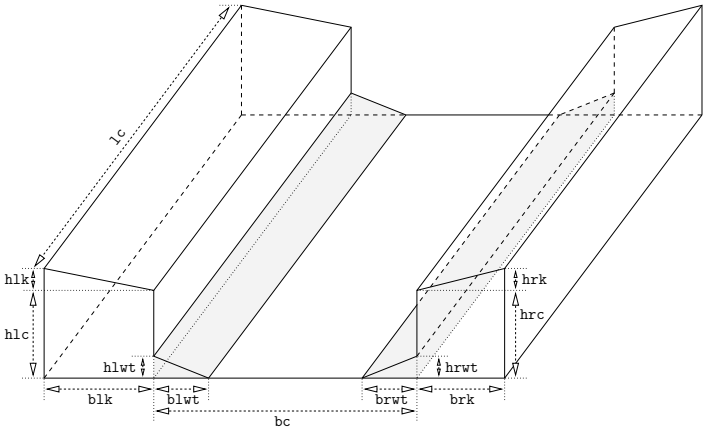

Figure A.2: Dimensions of the canal and quay.

The parameters from the canal and slope of the experimental model standard are given by (see Figure A.2):

	description	symbol	value ($2a/b$)
canal	length of canal	lc	8.5 m
	width of canal	bc	1.5 m
	height of left quay	hlc	0.246 m
	height of right quay	hrc	0.246 m
	width of left talus	blwt	0.0 m
	height of left talus	hlwt	0.0 m
	width of right talus	brwt	0.0 m
	height of right talus	hrwt	0.0 m
	height of water	hw	0.24 m
left slope	width of slope	blk	0.3 m
	height of slope	hlk	0.021 m
right slope	width of slope	brk	0.0 m
	height of slope	hrk	0.0 m
	width of talus	brkt	0.0 m
	height of talus	hrkt	0.0 m

Other test cases

Van Hooren did several experiments. In comparison with the *standard* cases $2a/2b$ only a few parameters change each time. For the diverse experiments the different parameters are:

model	a		b	
	parameter	value	parameter	value
1	V	0.3 m/s	V	0.3 m/s
2	std.		std.	
3	V	0.889 m/s	V	0.889 m/s
4	hlc	0.288 m	hs	0.042 m
5	hlc	0.257 m	hlk	0.032 m
			hs	0.042 m
6	hw	0.28 m	hlk	0.042 m
	hlc	0.297 m	hs	0.042 m
7	hlk	0.042 m	hlc	0.257 m
	hs	0.042 m		
8	hs	0.042 m	hlc	0.288 m
9	KG	0.194 m	hlc	0.267 m
	V	0.3 m/s		
10	KG	0.194 m	hw	0.28 m
			hlc	0.297 m
11	m	37.8 kg	KG	0.194 m
	V	0.3 m/s	V	0.3 m/s
12	m	37.8 kg	KG	0.194 m
			V	0.889 m/s
13			KG	0.194 m
14*			V	0.3 m/s
15*			V	0.6 m/s
16*			V	0.889 m/s
	* m = 58.8 kg, KG = 0.156 m and ix = 0.18 m			

There are many other parameters in the model, but they were not important to the experimental model and were thus also not investigated in the tests of Van hooren. For a more extensive explanation of (all) the model parameters refer to the user guide available at the department of mathematics of the *University of Groningen*.

Appendix B

Runge-Kutta coefficients

The in this project embedded Cash-Karp Runge-Kutta method uses the following coefficients for computation (see chapter 3.1.1). If a, b and c are given by:

$$\begin{array}{c|cccc} c_1 & & & & \\ \vdots & a_{2,1} & & & \\ \vdots & \vdots & \ddots & & \\ c_6 & a_{6,1} & \cdots & a_{6,5} & \\ \hline & b_1 & \cdots & \cdots & b_6 \end{array}$$

the fourth order scheme is:

$$\begin{array}{c|cccccc} 0 & & & & & & \\ \frac{1}{5} & \frac{1}{5} & & & & & \\ \frac{3}{10} & \frac{3}{40} & \frac{9}{40} & & & & \\ \frac{3}{5} & \frac{3}{10} & \frac{-9}{10} & \frac{6}{5} & & & \\ 1 & \frac{-11}{54} & \frac{5}{2} & \frac{-70}{27} & \frac{35}{27} & & \\ \frac{7}{8} & \frac{1631}{55296} & \frac{175}{512} & \frac{575}{13824} & \frac{44275}{110592} & \frac{253}{4096} & \\ \hline & \frac{37}{378} & 0 & \frac{250}{621} & \frac{125}{594} & 0 & \frac{512}{1771} \end{array}$$

where $y_{n+1} = y_n + b_1 k_1 + \ldots + b_6 k_6 + O(dt^5)$ and for the fifth order scheme:

$$\begin{array}{c|cccccc} 0 & & & & & & \\ \frac{1}{5} & \frac{1}{5} & & & & & \\ \frac{3}{10} & \frac{3}{40} & \frac{9}{40} & & & & \\ \frac{3}{5} & \frac{3}{10} & \frac{-9}{10} & \frac{6}{5} & & & \\ 1 & \frac{-11}{54} & \frac{5}{2} & \frac{-70}{27} & \frac{35}{27} & & \\ \frac{7}{8} & \frac{1631}{55296} & \frac{175}{512} & \frac{575}{13824} & \frac{44275}{110592} & \frac{253}{4096} & \\ \hline & \frac{2825}{27648} & 0 & \frac{18575}{48384} & \frac{13525}{55296} & \frac{277}{14336} & \frac{1}{4} \end{array}$$

where $y^*_{n+1} = y_n + b^*_1 k_1 + \ldots + b^*_6 k_6 + O(dt^6)$ and the coefficients $k_1, \ldots k_6$ are given by:

$$\begin{aligned} k_1 &= dt\ f(t + c_1\ dt, y_n) \\ k_2 &= dt\ f(t + c_2\ dt, y_n + a_{2,1}\ k_1) \\ &\cdots \\ k_6 &= dt\ f(t + c_6\ dt, y_n + a_{6,1}\ k_1 + \ldots + a_{6,5}\ k_5) \end{aligned}$$

and the error estimate is $\Delta y \equiv y_{n+1} - y^*_{n+1} = \sum_{i=1}^{6} (b_i - b^*_i) k_i$.

Appendix C

Figures of Chapter 4

In chapter four serveral simulations were done. Figures of y-position, z-position and rotation angle ϕ are given in this appendix.

Grid refinement

Standard tests

Tests with altered parameters

Additional tests

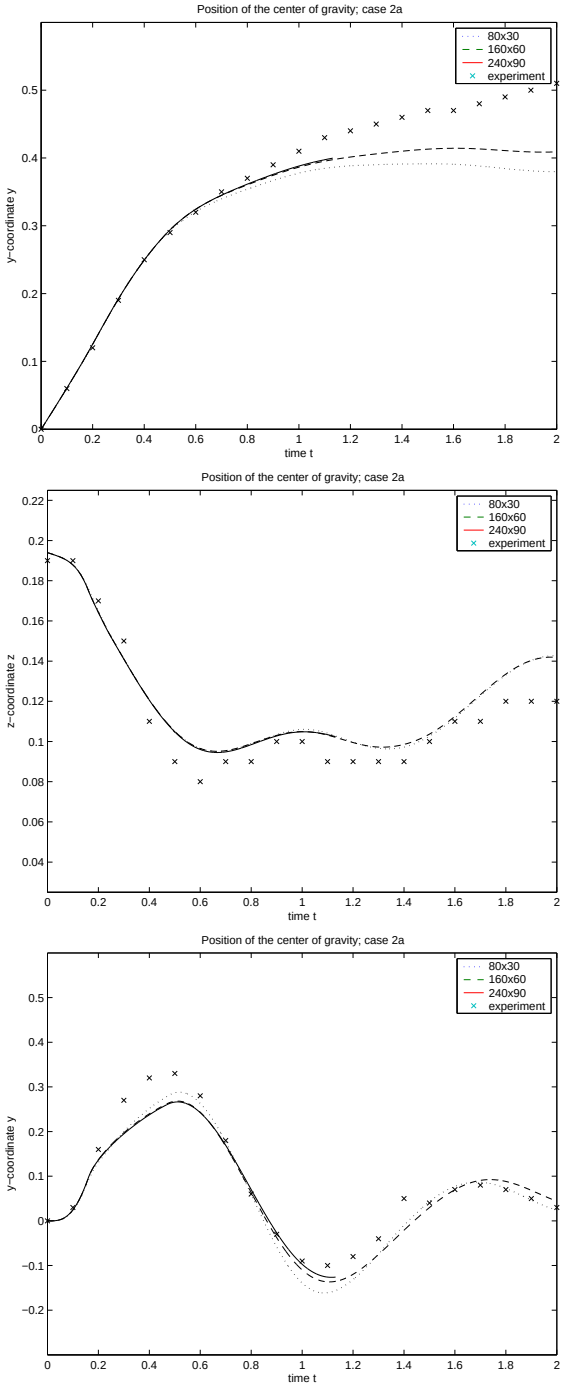

Figure C.1: Two dimensional grid refinement of test case $2a$; $2D$.

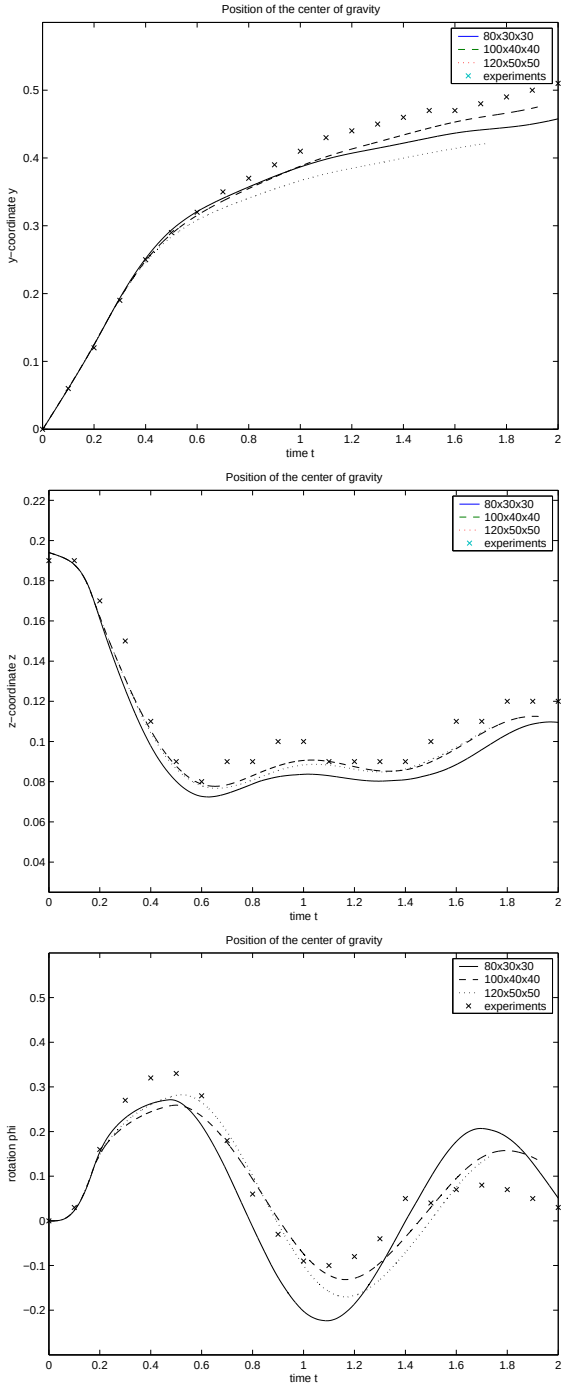

Figure C.2: Three dimensional grid refinement of test case $2a$; $3D$.

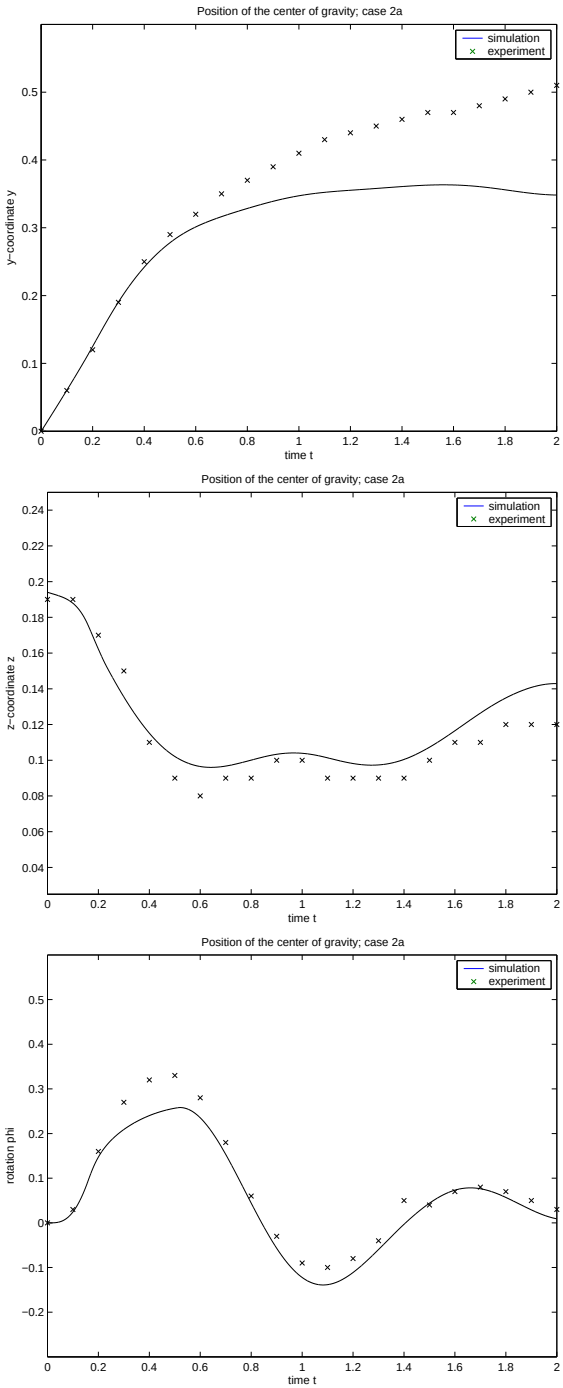

Figure C.3: Position and rotation of test case $2a$; $2D$.

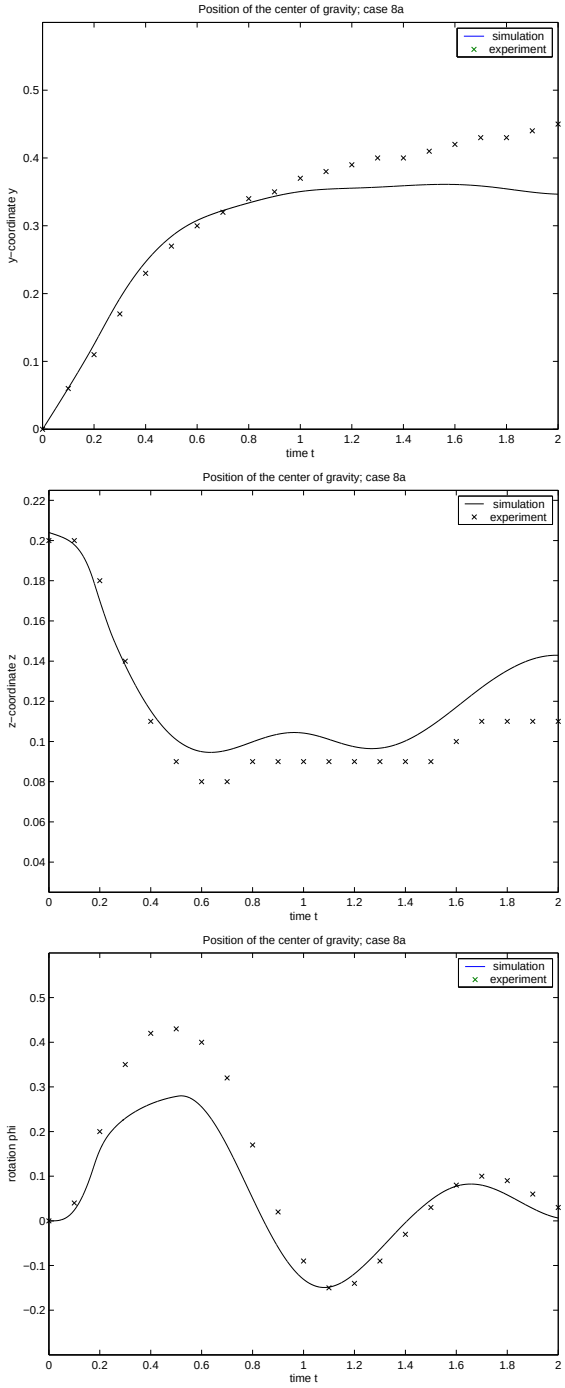

Figure C.4: Position and rotation of test case $8a$; $2D$.

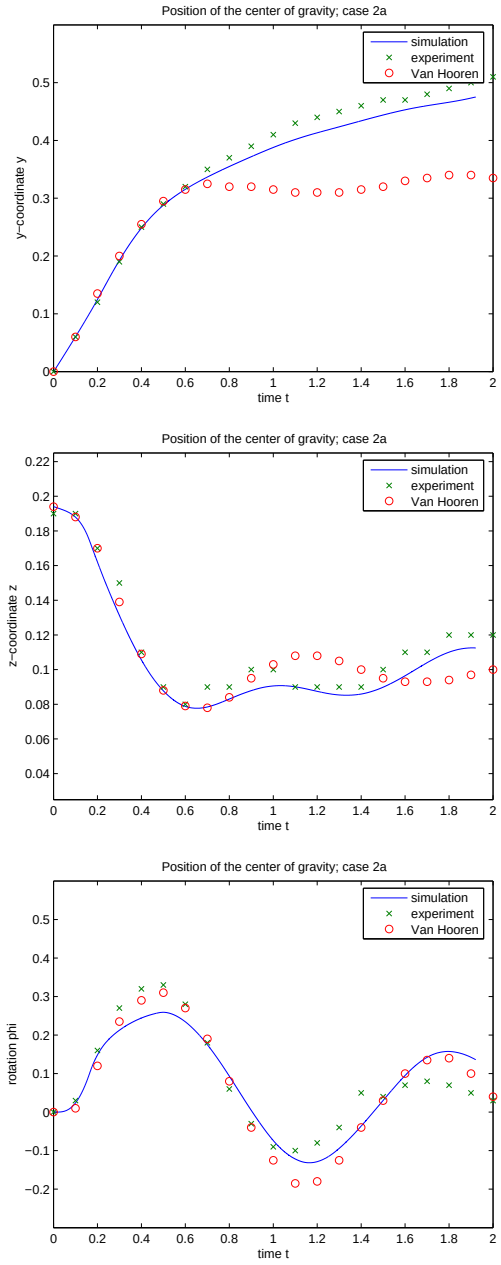

Figure C.5: Position and rotation of test case $2a$; $3D$.

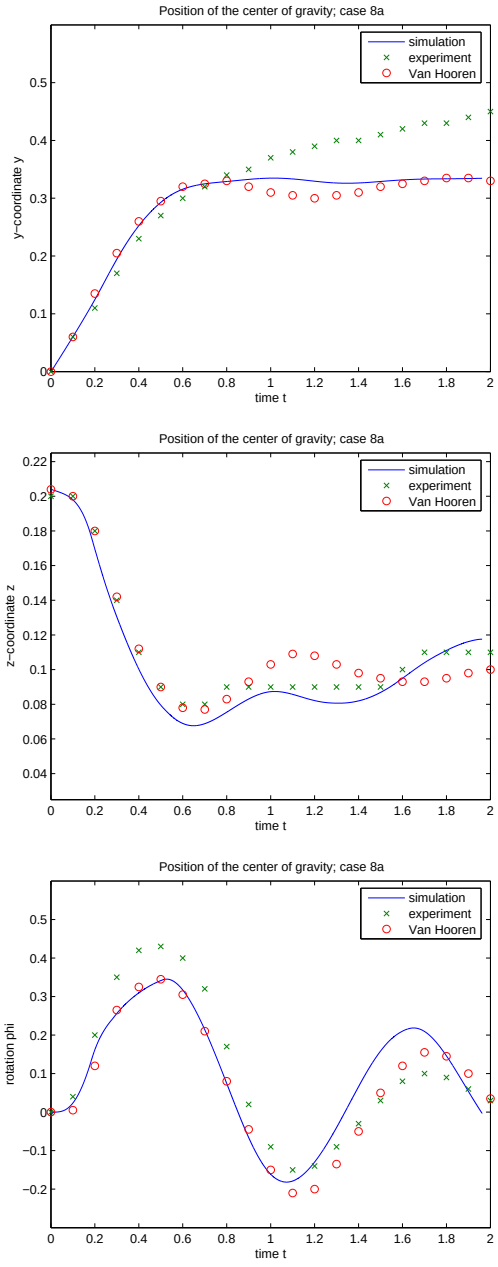

Figure C.6: Position and rotation of test case $8a$; $3D$.

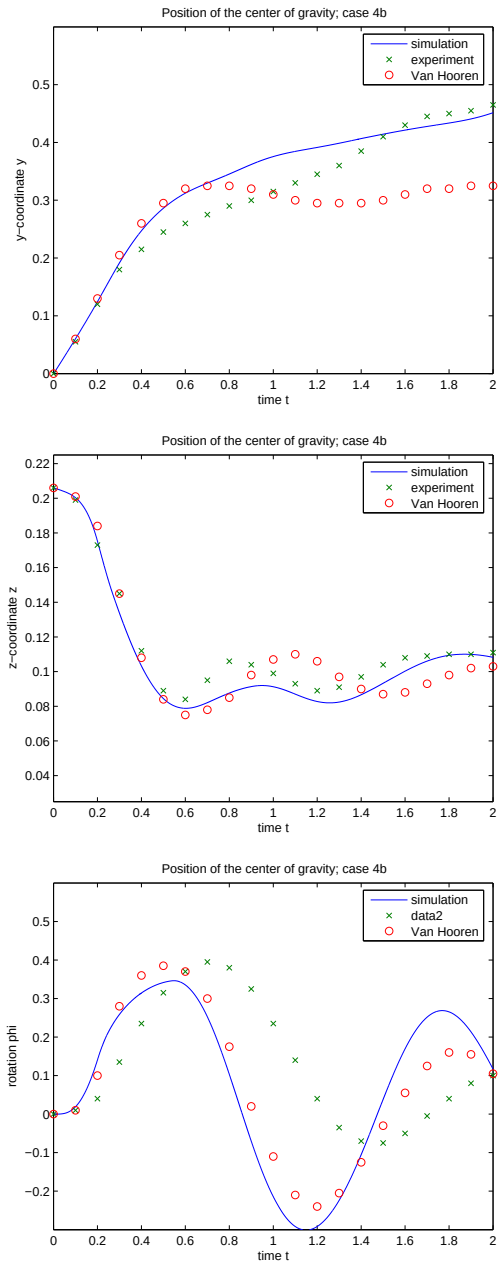

Figure C.7: Position and rotation of test case 4*b*.

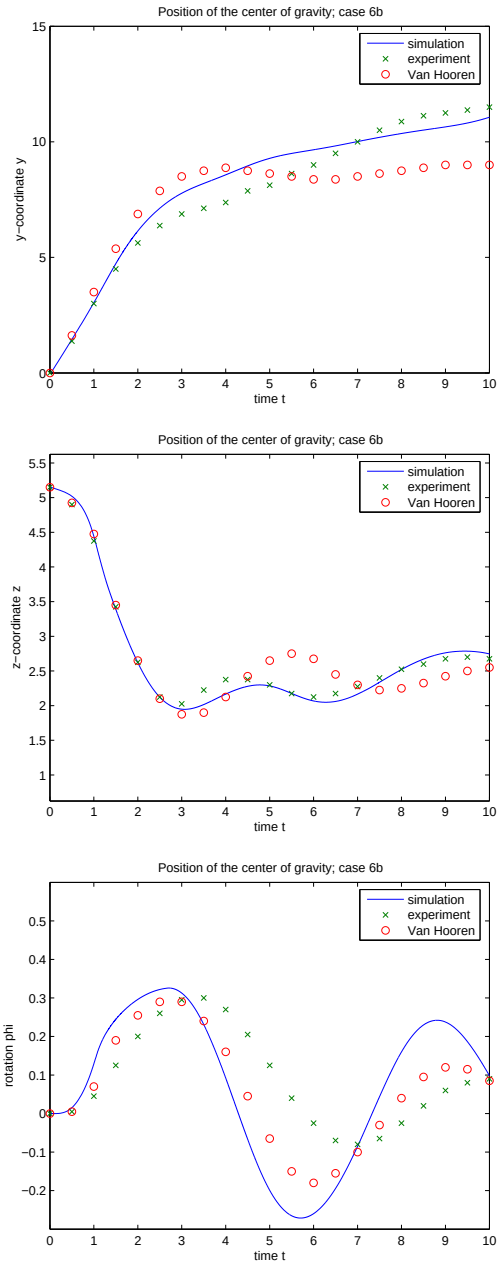

Figure C.8: Position and rotation of test case 6*b*.

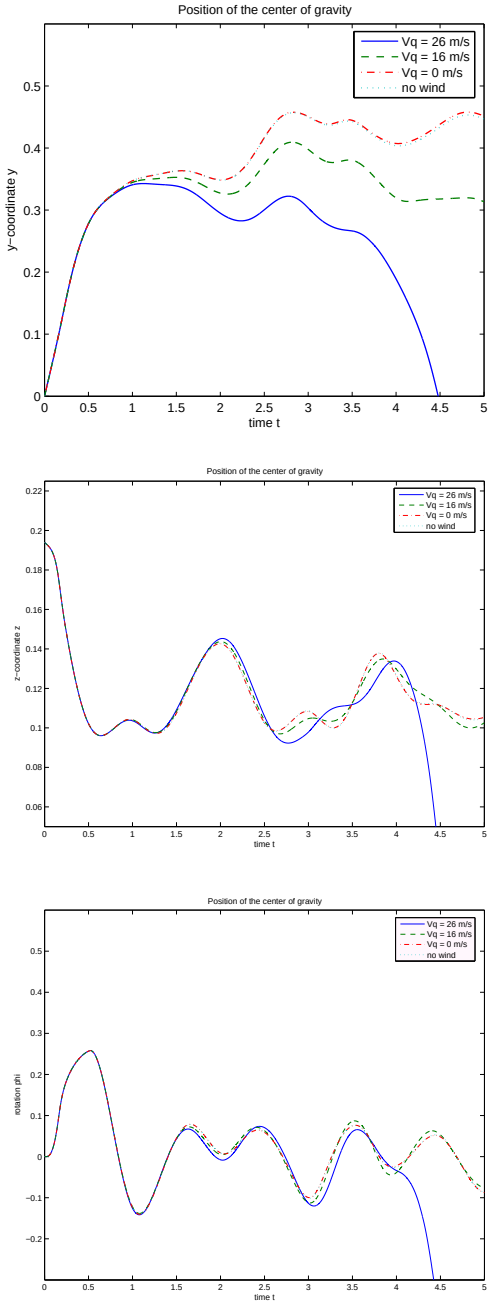

Figure C.9: Position and rotation of test case 2*a* including the wind model for different wind velocities.

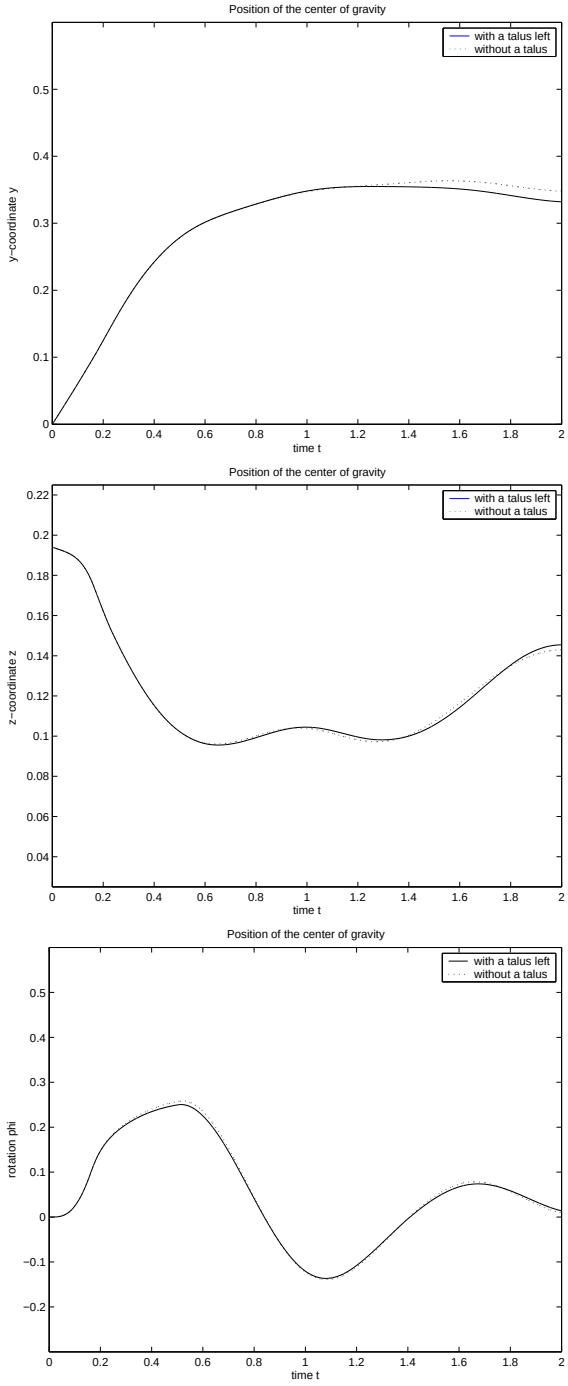

Figure C.10: Position and rotation of test case 2*a* using a talus on the left side of the quay.

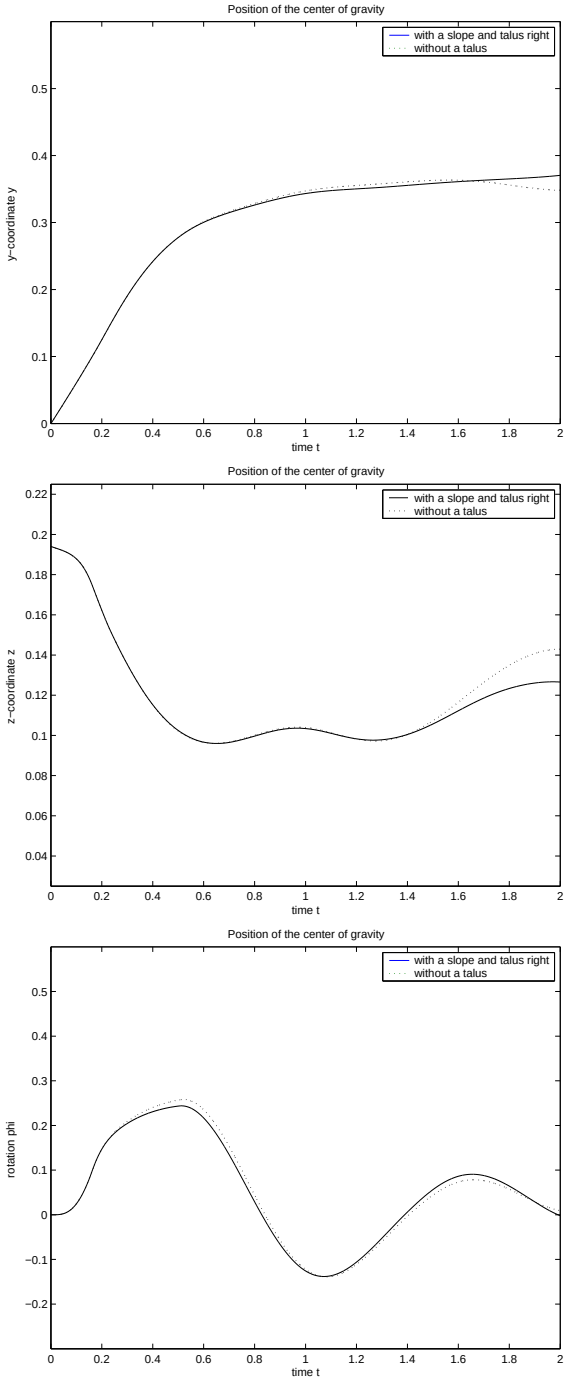

Figure C.11: Position and rotation of test case 2*a* using a talus and slope on the right side of the quay.

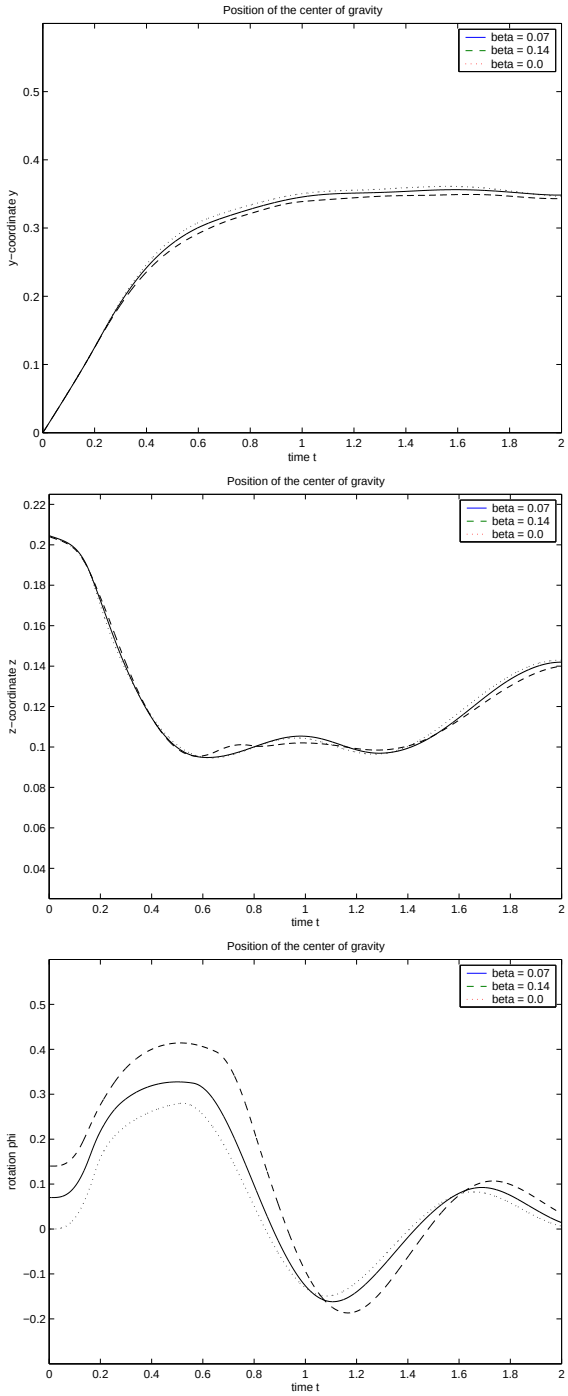

Figure C.12: Position and rotation of test case 8*a* with an initial angle.

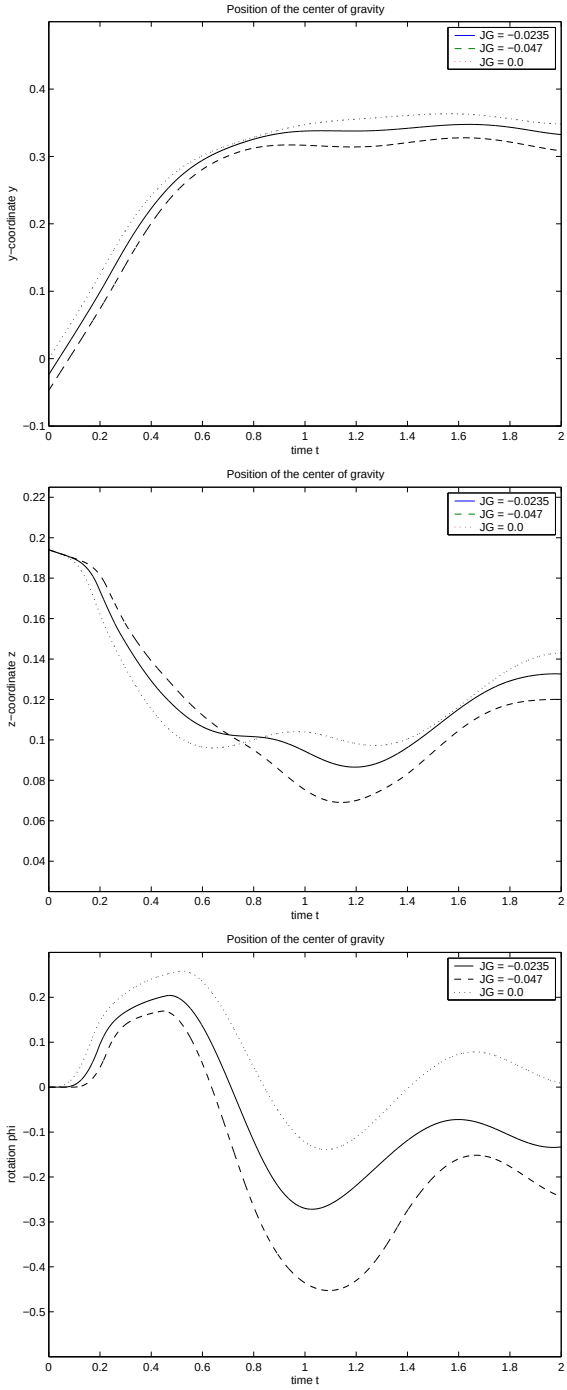

Figure C.13: Position and rotation of test case $2a$ with moved center of gravity.

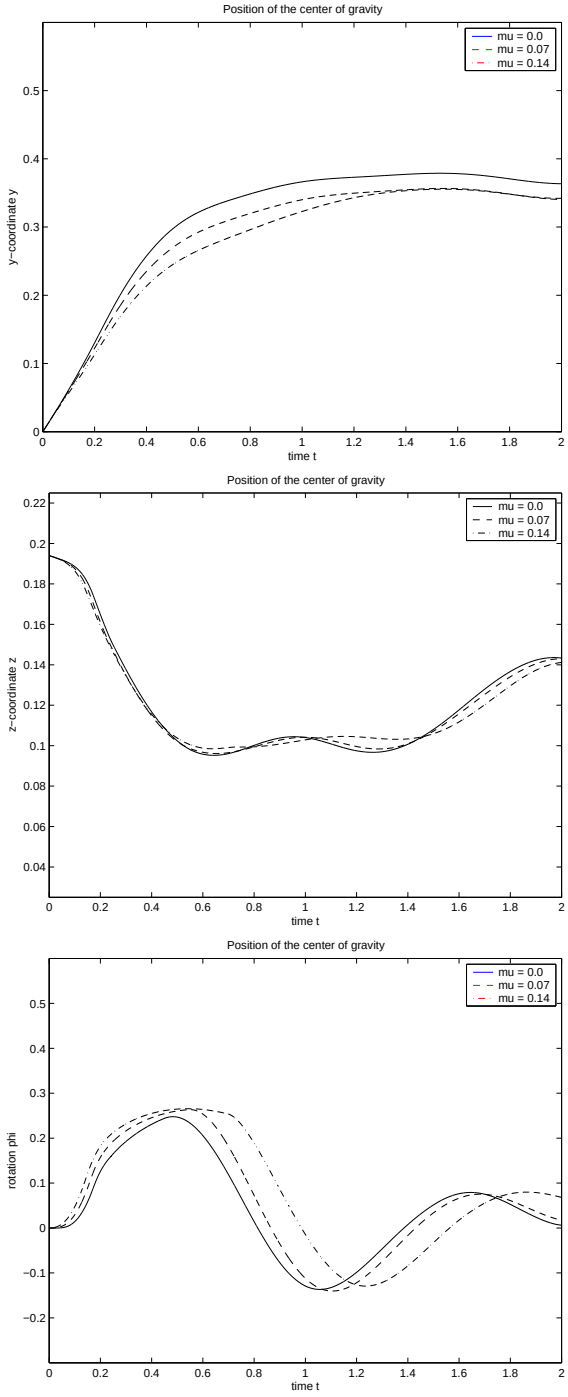

Figure C.14: Position and rotation of test case 2a with a different friction coefficient.

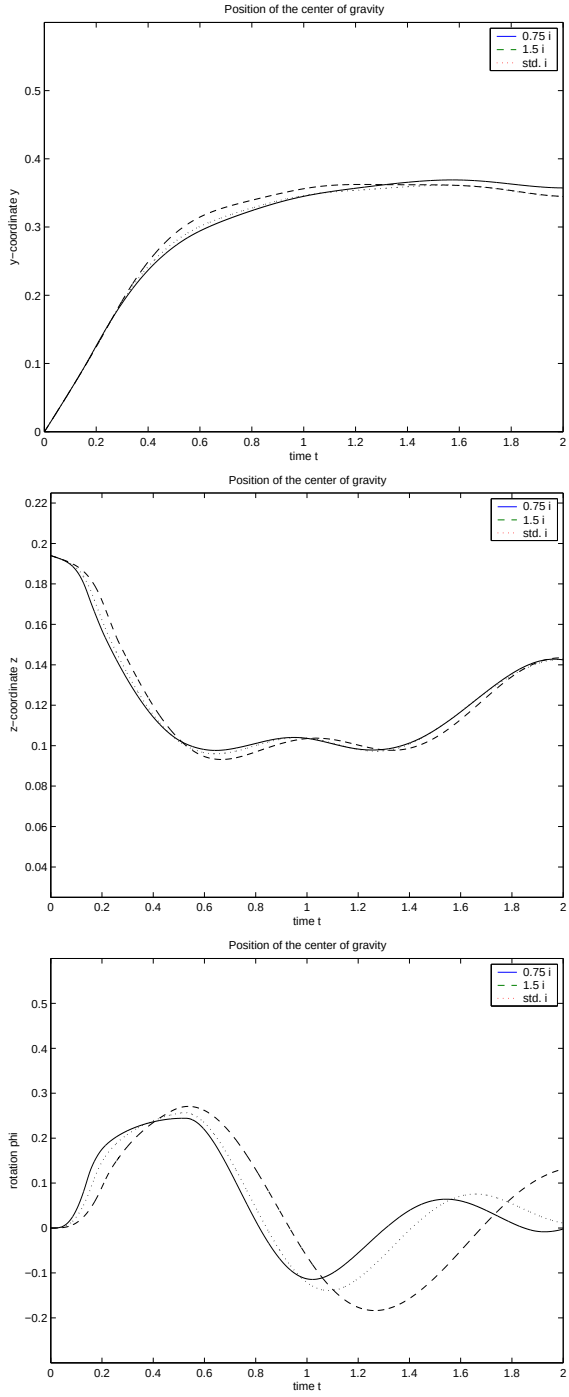

Figure C.15: Position and rotation of test case 2a with different radius of inertia.

Bibliography

[1] K.E. Atkinson, *An Introduction to Numerical Analysis*, John Wiley & Sons, Inc., 1989

[2] J.C. Butcher, *The Numerical Analysis of Ordinary Differential Equations*, John Wiley & Sons Ltd., 1987

[3] E.F.F. Botta and M.H.M. Ellenbroek, *A modified SOR method for the poison equation in unsteady free-surface flow calculations*, Journal of Computational Physics, **60** p119-p134, 1985

[4] J.R. Cash and A.H. Karp, *A variable order Runge-Kutta method for initial value problems with rapidly varying right-hand sides*, ACM Trans. Math. Softw. **16**, p201-p222, 1990

[5] G. Fekken, *Numerical Simulation of Greenwater Loading on the Foredeck of a Ship*, Master Thesis, University of Groningen, August 1998

[6] G. Fekken, *Numerical simulation of free-surface flow with moving rigid bodies*, PhD Thesis, University of Groningen, 2004

[7] J. Gerrits, *Dynamics of liquid-filled spacecraft*, PhD Thesis, University of Groningen, 2001

[8] J.A. Keuning and C.J. Bom, *Geometrie en Stabiliteit*, Internal notes of the *TU Delft*, 2001

[9] Chr. M. van Hooren, *Dwarsscheeps tewaterlaten. Berekening met behulp van een computer. Modelproeven.*, Technical Report 297-M of the laboratorium for shipbuilding of the Technische Hogeschool Delft, January 1971

[10] Ju. S. Jakovlev, *Berekeningen en experimentele proeven van opdrijven, stabiliteit en tewaterlating* (translation from Russian), Technical Report, 1947

[11] P. de Jong, *Numerical simulation of the side launching of a ship*, Master thesis, March 2004

[12] Z. Meglicki, *Advanced Scientific Computing*, Lecture Notes of Course **B673**, 2001

[13] A.E.P. Veldman, *Computational Fluid Dynamics*, Lecture Notes, September 2001

[14] J. Versluis, *Ontwerp modelopstelling voor systematies onderzoek dwarsaflopen schepen*, Technical Report of the laboratorium for shipbuilding of the Technische Hogeschool Delft, 1968